

André Luis Pires de Oliveira

**Harmonic Compensation Strategies Applied
to Photovoltaic Inverters into Distribution
Radial Lines**

Viçosa, MG

2021

André Luis Pires de Oliveira

Harmonic Compensation Strategies Applied to Photovoltaic Inverters into Distribution Radial Lines

Monografia apresentada ao Departamento de Engenharia Elétrica do Centro de Ciências Exatas e Tecnológicas da Universidade Federal de Viçosa, para obtenção dos créditos referentes à disciplina ELT 402 - Projeto de Engenharia II e cumprimento do requisito parcial para obtenção do grau de Bacharel em Engenharia Elétrica.

Universidade Federal de Viçosa

Departamento de Engenharia Elétrica

Curso de Graduação em Engenharia Elétrica

Orientador: Prof. Dr. Heverton Augusto Pereira

Coorientador: Me. João Marcus Soares Callegari

Viçosa, MG

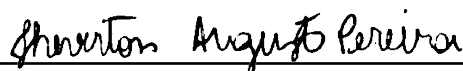
2021

André Luis Pires de Oliveira

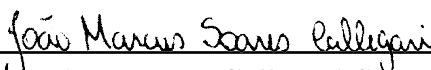
Harmonic Compensation Strategies Applied to Photovoltaic Inverters into Distribution Radial Lines

Monografia apresentada ao Departamento de Engenharia Elétrica do Centro de Ciências Exatas e Tecnológicas da Universidade Federal de Viçosa, para obtenção dos créditos referentes à disciplina ELT 402 - Projeto de Engenharia II e cumprimento do requisito parcial para obtenção do grau de Bacharel em Engenharia Elétrica.

Trabalho aprovado. Viçosa, MG, 24 de maio de 2021:



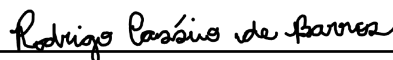
Prof. Dr. Heverton Augusto Pereira
Orientador



Me. João Marcus Callegari Soares
Coorientador



Me. Lucas Santana Xavier
Convidado 1



Me. Rodrigo Cássio de Barros
Convidado 2

Viçosa, MG

2021

À minha família, mentores e amigos.

Agradecimentos

Em primeiro lugar, agradeço infinitamente aos meus pais, Eva e Paulo, e a minha irmã, Larissa, por me darem todo o amor, suporte e confiança necessários para chegar até aqui. Saibam que essa conquista jamais seria possível sem a presença de vocês. Deixo registrado minha eterna gratidão.

Agradeço imensamente a minha namorada, Carolina, que esteve presente em toda essa jornada. Palavras não são suficientes para agradecer todo o amor, carinho, companheirismo, confiança e auxílio depositados nessa caminhada. Me espelho em sua determinação e força de vontade. Cada dia mais sua presença se torna essencial para minha vida.

Agradeço à Universidade Federal de Viçosa (UFV) e ao Departamento de Engenharia Elétrica por todo o suporte fornecido durante minha formação acadêmica. Um agradecimento especial à Gerência de Especialistas em Sistemas Elétricos de Potência (GESEP-UFV) pelas oportunidades, por alinhar minha trajetória e abrir novos caminhos para meu crescimento acadêmico e profissional.

Agradeço ao meu orientador Prof. Heverton pelo auxílio e confiança depositados nesse trabalho e por todos conhecimentos compartilhados, que foram fundamentais para meu desenvolvimento pessoal e acadêmico. Agradeço também ao Prof. Allan e ao Lucas Xavier por todos ensinamentos que tanto contribuíram na minha evolução acadêmica e na construção desse trabalho. Aproveito a oportunidade para agradecer também a todos os membros do GESEP que de alguma forma contribuíram na minha jornada.

Um agradecimento mais que necessário ao meu coorientador João Marcus, com quem tive imenso prazer de trabalhar diretamente. Agradeço por toda a disponibilidade e atenção dados à esse trabalho (sei que as dúvidas foram muitas) e por todo aprendizado. Com certeza você é uma referência para mim e um dos maiores contribuintes do meu crescimento pessoal e profissional.

Por fim, mas não menos importante, agradeço a todos meus amigos e colegas da ELT16 que se fizeram presentes em toda minha graduação. Em especial, ao Uliana, João Roberto, DB e LH por todo apoio, amizade e momentos compartilhados.

*“Pense que isso é uma corrida onde não importa a volta
e não importa quem vai chegar em primeiro
e sim onde tu quer chegar, qual tua meta? Mostra! “*
(Abebe Bikila)

Resumo

Os sistemas solares fotovoltaicos (FV) vêm se destacando cada vez mais na geração de energia elétrica ao redor do mundo. Sua integração, por meio de interfaces de geração distribuída, vem aumentando sua inserção nas mais diversas camadas dos sistemas elétricos de potência (SEP). Paralelo a esse fato, o aumento na conexão ao SEP de cargas não-lineares vem causando a proliferação de conteúdo harmônico nas linhas, reduzindo a qualidade do fornecimento de energia. Especialmente no nível de distribuição, a circulação de correntes harmônicas se torna um problema maior pois os efeitos sobre a qualidade da energia são mais evidentes, devido ao aumento das perdas nas linhas, distorções nas tensões, saturação de dispositivos magnéticos, excitação de ressonâncias intrínsecas do SEP, dentre outros efeitos. Nesse contexto, devido a característica intermitente da geração fotovoltaica, diversos trabalhos na literatura vêm discutindo a possibilidade de utilizar a margem de corrente dos sistemas fotovoltaicos para fornecer o serviço auxiliar de compensação harmônica (CH) embarcada ao inversor. Para integração desse serviço, é importante garantir que a corrente do inversor FV não extrapole o seu valor de pico nominal. Para esse propósito, técnicas de saturação dinâmica de corrente são adotadas, incorporando a capacidade de CH parcial aos inversores FV. Tendo em vista os pontos acima mencionados, esse trabalho propõe a implementação da CH parcial aplicada a múltiplos inversores FV monofásicos usando uma técnica de saturação dinâmica baseada em um algoritmo de malha aberta. Duas estratégias de CH são empregadas para análise e comparação dos seus efeitos e características, uma baseada na medição de tensão do ponto de acoplamento comum (PCC) do inversor com a rede elétrica e outra baseada na medição das correntes harmônicas das cargas. Para a técnica baseada na medição de tensão local, uma metodologia para ajuste do ganho que garante a estabilidade do sistema é apresentada. Uma linha de distribuição trifásica de baixa tensão em configuração radial é usada para analisar os efeitos do compartilhamento da CH entre os inversores FV. Simulações são implementadas no *software* PLECS para avaliar a CH parcial e comparar as duas estratégias empregadas. A performance das duas estratégias em uma condição em que os inversores FV tinham margem de corrente para CH total para duas condições de rede diferentes foi avaliada inicialmente. Posteriormente, o comportamento dinâmico das estratégias de CH com o algoritmo de saturação de corrente foi estudado, durante variações da irradiância solar sobre a superfície dos módulos FV. Os resultados da simulação mostram que a estratégia baseada em corrente apresenta maiores melhorias na qualidade da energia em redes mais rígidas, enquanto a estratégia baseada em tensão apresenta um desempenho melhor em redes mais fracas. Os resultados dinâmicos mostram a eficiência da estratégia de saturação dinâmica em manter a corrente dos conversores dentro dos limites nominais. Uma tabela comparativa sintetiza os resultados e principais características das duas técnicas de CH avaliadas.

Palavras-chaves: Inversores fotovoltaicos, controle, compensação harmônica, saturação dinâmica, qualidade de energia.

Abstract

The solar photovoltaic (PV) systems have been standing out each time more in electrical generation all over the world. Its integration, by distributed generation interfaces, have been increasing PV systems insertion in the most diverse levels of electrical power systems (EPS). Parallel to this fact, the increase connection into the EPS of nonlinear loads have been causing harmonic content proliferation through the power lines, reducing the power supply quality. Especially in distribution level, the harmonic current circulation becomes a bigger issue since the effects over power quality are more evident due to the increased losses in the power line, voltages distortions, saturation of magnetic devices, excitation of intrinsic resonances of SEP, among other effects. In this context, due to the PV generation intermittent nature, several works on literature have been discussing the possibility of using the PV inverters current margin to provide the harmonic compensation (HC) ancillary services embedded into the inverter. For integrating this services, it is important to ensure that the PV inverter current does not extrapolate its nominal peak value. For this purpose, dynamic current saturation techniques are employed, incorporating the partial HC capacity into the PV inverters. In view of the points aforementioned, this work proposes the implementation of partial HC applied to multiple single-phase PV inverters using a dynamic saturation based on an open-loop algorithm. Two HC strategies are employed for analysis and comparison of their effects and features, one based on measurement of the voltage on the point of coupling between the inverter and the electrical grid and the other based on loads harmonic currents measurement. For the scheme based on local voltage measurements, a methodology for tuning the gain that ensures system stability is presented. A low-voltage three-phase distribution line on radial configuration is used for analyzing the effects of the HC sharing between the PV inverters. Simulations are implemented on software PLECS for evaluating and comparing the two employed strategies. Both strategies performance for a condition which the PV inverters had current margin for total HC in two different grid conditions were evaluated at first. Subsequently, the HC strategies dynamic behaviour with the current saturation algorithm was studied during variations of solar irradiance over the PV modules. The simulation results shows that the current-based strategy presents higher improvements on power quality for more stiff grids, while the voltage-based strategy performs better in weaker grids condition. The dynamic results shows the dynamic saturation efficiency in keeping the PV inverters current within their rating limits. A comparative table summarizes the results and main features of the two analyzed HC techniques.

Key-words: Photovoltaic inverter, control, harmonic compensation, dynamic saturation, power quality.

List of Figures

Figure 1 – Estimated global growth in renewable energy compared to total final energy consumption, from 2013 to 2018 (REN 21, 2020).	27
Figure 2 – Renewable power capacity growth from 2015 to 2019 (IRENA, 2020). . .	28
Figure 3 – Typical electrical power system, with distributed generator and nonlinear load. Depending on the grid short-circuit capacity, high harmonic distortions in the PCC can occur.	30
Figure 4 – Overview of strategies proposed in the literature to grid power quality improvements using VSI's.	31
Figure 5 – Schematic of a two-stage single-phase grid-connected PV system. . . .	37
Figure 6 – (a) Boost converter control block diagram. (b) Inverter fundamental control block diagram.	38
Figure 7 – (a) Inverter with HC capability control block diagram. (b) Dynamic saturation block diagram.	41
Figure 8 – Simplified PV system for modelling purposes.	43
Figure 9 – Conventional HC strategy: (a) Equivalent circuit closed-loop representation. (b) Bode plot of the transfer function $k_{cl}(s)$. (c) Bode plot of the transfer function $1/Z_{cl}(s)$	45
Figure 10 – Local voltage-based HC strategy: (a) Equivalent circuit closed-loop representation, (b) Bode plot of the transfer function $1/Z_h(s)$, (c) Zoomed view of the bode plot $1/Z_h(s)$	47
Figure 11 – Local voltage-based HC strategy stability analysis. (a) Stability limit curve. (b) Closed-loop transfer functions poles. (c) Zoomed view on the stable region limit.	49
Figure 12 – Inverter reference current waveform and the injected current spectrum. (a) Conventional saturation. (b) Dynamic saturation.	51
Figure 13 – Single-phase grid-connected PV systems into the case study radial distribution line.	54
Figure 14 – Current spectra of the nonlinear load used in the case study.	56
Figure 15 – Case study solar irradiance profile on PV arrays connected to the (a) inverter 1, (b) inverter 2, (c) inverter 3.	58
Figure 16 – Weak grid HC strategies evaluation: (a) Local current-based HC scheme. (b) Local voltage-based HC scheme.	62
Figure 17 – Stiff grid HC strategies evaluation: (a) Local current-based HC scheme. (b) Local voltage-based HC scheme.	63

Figure 18 – Local current-based HC strategy evaluation: (a) Compensation factor K_h . (b) TDD of the PCC current i_{pcc} . (c) THD of the PCC voltage v_{pcc} . (d) PCC current dynamic.	65
Figure 19 – Local current-based HC strategy evaluation: (a) Inverter-1 current dynamic. (b) Inverter-2 current dynamic. (c) Inverter-3 current dynamic.	66
Figure 20 – Local voltage-based HC strategy evaluation: (a) Compensation factor K_h . (b) TDD of the PCC current i_{pcc} . (c) THD of the PCC voltage v_{pcc} . (d) PCC current dynamic.	68
Figure 21 – Local voltage-based HC strategy evaluation: (a) Inverter-1 current dynamic. (b) Inverter-2 current dynamic. (c) Inverter-3 current dynamic.	69

List of Tables

Table 1 – Parameters of the three-phase star-connected (Y) and single-phase loads.	53
Table 2 – Distribution line impedance values.	54
Table 3 – Parameters of the multiple single-phase PV inverters and nonlinear loads connected into the radial line.	55
Table 4 – PV module parameters.	56
Table 5 – Parameters of the controllers for the single-phase PV systems.	57
Table 6 – Comparison between the HC techniques.	70

List of abbreviations and acronyms

AC	Alternating Current
APF	Active Power Filters
CCM	Current-controlled Mode
CPT	Conservative Power Theory
CS	Conventional Saturation
DC	Direct Current
DPGS	Distributed Power Generation Systems
dq	Synchronous Reference Frame
DS	Dynamic Saturation
EPS	Electric Power System
HC	Harmonic Compensation
HCFC	Harmonic Compensation Factor Calculation
HD	Harmonic Detection
HVD	Harmonic Voltage Detector
IEEE	Institute of Electrical and Electronics Engineers
IIR	Infinite-Impulse Response
LPF	Low-pass Filter
LV	Low Voltage
MPPT	Maximum Power Point Tracking
PCC	Point of Common Coupling
PI	Proportional-integral
PLL	Phase-locked Loop
PMR	Proportional Multi-resonant

PoC	Point of Connection
PR	Proportional-resonant
PV	Photovoltaic
PWM	Pulse Width Modulation
P&O	Perturb and Observe
RMS	Root Mean Square
R-APF	Resistive Active Power Filters
SOGI	Second-order Generalized Integrator
SPWM	Sinusoidal PWM
SRF-PLL	Synchronous Reference Frame PLL
TDD	Total Demand Distortion
TFEC	Total Final Energy Consumption
THD	Total Harmonic Distortion
VCM	Voltage-controlled Mode
VSI	Voltage Source Inverter

List of symbols

C_{dc}	DC-link capacitance
C_f	LCL filter capacitance
C_i	PV module temperature coefficient of the short-circuit current
C_{NL}	Nonlinear load capacitance
C_{pv}	PV arrays output capacitance
C_v	PV module temperature coefficient of the open-circuit voltage
d^*	Boost converter duty cycle reference
f_n	Nominal grid frequency
f_{res}	LCL filter resonance frequency
f_{sw}	Inverter switching frequency
f_s	Inverter sampling frequency
f_{swb}	Boost converter switching frequency
$F_{BP}(s)$	Transfer function of the band-pass filter
$F_{NT}(s)$	Transfer function of the notch filter
G_n	PV module nominal irradiance
$G_c(s)$	Transfer function of the current controller for harmonic compensation
$G_{i,1}(s)$	Transfer function of the current stability analysis for local current-based harmonic compensation strategy
$G_{i,2}(s)$	Transfer function of the current stability analysis for local voltage-based harmonic compensation strategy
$G_{PR}(s)$	Transfer function of the current controller
$G_{v,1}(s)$	Transfer function of the voltage stability analysis for local current-based harmonic compensation strategy
$G_{v,2}(s)$	Transfer function of the voltage stability analysis for local voltage-based harmonic compensation strategy

G_x	Solar irradiance on PV system x
$G_1(s)$	Transfer function of inverter output voltage and output current relation
$G_2(s)$	Transfer function of inverter output voltage and grid voltage relation
h	Harmonic order
$H(s)$	Transfer function of PWM delay
$H_d(s)$	Transfer function of harmonic detector
i_g	Grid current
$i_{g,x}$	Output current on point of connection x
i_L	Nonlinear load current
i_{Lb}	Boost converter input current
i_{mpp}	PV module current at maximum power point
i_o	Inverter output current (Grid side)
i_{pcc}	Point of common coupling current
i_{pv}	PV arrays output current
i_s	Inverter output current (Converter side)
i_{sc}	PV module short-circuit current
i^*	Inverter current reference without saturation
i_α^*	Inverter fundamental current reference
i_h^*	Inverter harmonic current reference
i_{Lb}^*	Boost converter input current reference
i_s^*	Inverter output current (Converter side) reference
$i_{s,h}^*$	Inverter harmonic current reference after saturation
I_α	Fundamental component contribution to the inverter peak value
I_h	Harmonic component contribution to the inverter peak value
I_m	Peak value of the inverter current reference
I_{max}	Inverter peak rated current

$I_{x,h}$	x node current harmonic component
I_m^*	Inverter rated current
$k(s)$	Transfer function of inverter open-loop natural gain
$k_{cl}(s)$	Transfer function of inverter closed-loop natural gain
K_h	Harmonic compensation factor
K_p	Current controller proportional gain
$K_{r,f}$	Current controller fundamental resonant gain
$K_{r,h}$	Current controller harmonic resonant gain
K_v	Local voltage-based harmonic compensation gain
L_a	Phase A load inductance
L_b	Phase B load inductance
L_{boost}	Boost converter inductance
L_c	Phase C load inductance
$L_{d,y}$	Point of connection y distribution line inductance
$L_{g,x}$	Node x grid line inductance
L_g	Grid equivalent inductance
L_{NL}	Nonlinear load inductance
L_1	LCL filter inductance (Inverter side)
L_2	LCL filter inductance (Grid side)
n_s	PV module number of cells in series
N_p	PV array number of parallel connected PV modules
N_s	PV array number of series connected PV modules
ω_b	Notch filter bandwidth
ω_{c1}	Band-pass filter lower band cut-off frequency
ω_{c2}	Band-pass filter upper band cut-off frequency
ω_f	Fundamental angular frequency

ω_h	Harmonic angular frequency
P_{mpp}	PV module maximum power
P_{max}	PV array rated power
P_{pv}	Active power generated by PV arrays
PWM_{boost}	Boost converter PWM signal
PWM_{inv}	Inverter PWM signals
P^*	Active power reference injected by inverter
Q^*	Reactive power reference injected by inverter
r_b	Boost converter inductor resistance
R_a	Phase <i>A</i> load resistance
R_b	Phase <i>B</i> load resistance
R_c	Phase <i>C</i> load resistance
R_d	Filter damping resistance
$R_{d,y}$	Point of connection <i>y</i> distribution line resistance
R_g	Grid equivalent resistance
$R_{g,x}$	Node <i>x</i> grid line resistance
R_{LNL}	Nonlinear load inductor resistance
R_{NL}	Nonlinear load resistance
R_p	PV module parallel resistance
R_s	PV module series resistance
S_{max}	Inverter rated power
$T_{a,x}$	Ambient temperature on PV system <i>x</i>
T_d	PWM scheme delay
T_n	PV module nominal operation temperature
T_s	Inverter sampling period
T_{sw}	Inverter switching period

$v_{\alpha,\beta}$	Grid voltage in stationary reference-frame
v_{dc}	DC-link voltage
v_g	Grid voltage
v_{mpp}	PV module voltage at maximum power point
v_o	Inverter output voltage (Grid side)
v_{oc}	PV module open-circuit voltage
$v_{o,x}$	Voltage of point of connection x
v_{pcc}	Point of common coupling voltage
v_{pv}	PV arrays output voltage
v_s	Inverter output voltage (Converter side)
v_{dc}^*	DC-link voltage reference
v_{pv}^*	PV arrays output voltage reference
v_s^*	Inverter output voltage (Converter side) reference
$V_{x,h}$	x node voltage harmonic component
$V_{x,h}$	x node voltage fundamental component
X/R	Reactance and resistance relation
$Z_{cl}(s)$	Transfer function of inverter closed-loop output impedance
Z_C	Filter capacitor branch impedance
$Z_{d,y}$	Point of connection y distribution line impedance
$Z_{eq}(s)$	Transfer function of inverter closed-loop equivalent output impedance
Z_g	Grid impedance
$Z_h(s)$	Transfer function of inverter closed-loop harmonic output impedance
$Z_{th}(s)$	Transfer function of inverter open-loop output impedance
Z_1	Converter-side inductor impedance
Z_2	Grid-side inductor impedance

Contents

1	INTRODUCTION	27
1.1	Objectives, Contributions and Limitations	34
1.2	Text Organization	35
1.3	Related Publication	35
2	METHODOLOGY	37
2.1	Single-Phase Double-Stage PV Systems	37
2.2	Harmonic Compensation Strategies	41
2.2.1	Conventional Harmonic Compensation Strategy	42
2.2.2	Local Voltage-Based Harmonic Compensation Strategy	45
2.2.3	Impedance-based Stability Analysis	47
2.3	Dynamic Saturation Scheme	50
2.4	Chapter Closure	52
3	PARTIAL HC APPLIED TO MULTIPLE PV INVERTERS: A CASE STUDY	53
3.1	Case Study System Description	53
3.2	Case Study Configurations	55
3.3	Chapter Closure	59
4	RESULTS AND DISCUSSION	61
4.1	Harmonic Compensation Strategies Evaluation	61
4.2	Case Study System Dynamic Evaluation	64
4.2.1	Local Current-based HC Strategy Evaluation	64
4.2.2	Local Voltage-based HC Strategy Evaluation	67
4.3	Chapter Closure	68
5	CONCLUSIONS	71
5.1	Research Perspectives	72
	REFERENCES	73

1 Introduction

In the 21st century, the effects in the natural environment of conventional fossil-based energies, such as coal, oil and natural gas, have become a major focus of discussion. Besides, the increasing demand for energy has led several countries around the world to invest in the development of renewable energies to diversify their energy matrices (REN 21, 2020). Fig. 1 shows the estimated global growth in renewable energy compared to total final energy consumption (TFEC) from 2013 to 2018. The 21,5 % growth in renewable energies in front of the growth of 5,7 % in conventional energies shows the trend toward diversification.

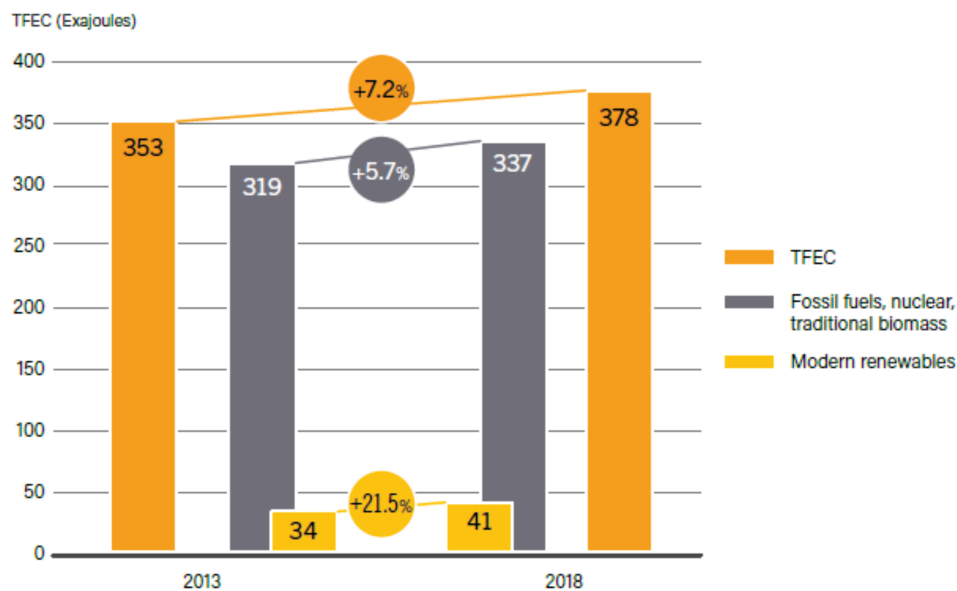


Figure 1 – Estimated global growth in renewable energy compared to total final energy consumption, from 2013 to 2018 (REN 21, 2020).

Ahead, Fig. 2 shows the renewable capacity growth between 2015 and 2019, where hydropower represents, at the end of 2019, 47 % of global total renewable capacity with 1190 GW. However, solar energy, which includes solar thermal and solar photovoltaic (PV) energy (being the latter the most significant), leads growth in 2019 with an increase of 98 GW (20%), followed by wind energy with 59 GW (10%). These values shows a clear domination of solar and wind energy in renewable capacity expansion, being responsible for 90% of net additional renewable in 2019 (IRENA, 2020).

PV systems have been standing out, mainly, due their decentralized generation capacity, cost reduction and increased efficiency of PV modules, ease of installation, increased environmental awareness and favorable local governments political regulation (Kouro et al., 2015). Typically, renewable energy sources are integrated in form of distributed

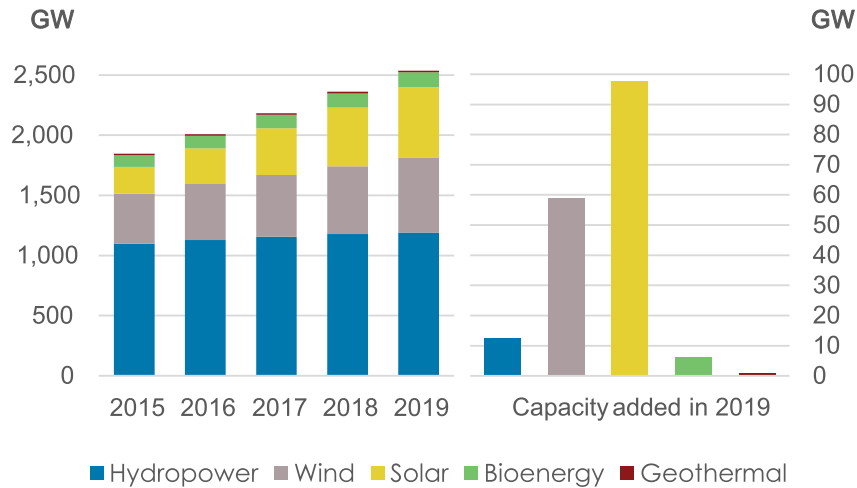


Figure 2 – Renewable power capacity growth from 2015 to 2019 (IRENA, 2020).

power generation systems (DPGS). This generation model allows a greater proximity between the energy and the consumer, reducing losses in transmission and distribution power lines (Blaabjerg et al., 2017). Parallel to the increasing penetration level of DPGS to the electric power system (EPS), arise new challenges related to grid operation and management to provide power-supply reliability and quality. The decentralized power sharing suffers with issues related to reverse power flow, voltage fluctuations and system resonance. A important device in the grid-connected PV system is the power inverter, responsible to perform the interface between the PV array and grid. In this context, the power-electronic technology has an important role in the integration, since inadequate DPGS control can lead to grid instability or failure (Blaabjerg et al., 2006a; Carrasco et al., 2006; Wang et al., 2011a).

In grid-connected PV systems, the intermittent energy generated by the PV plant is direct injected into the grid (Kouro et al., 2015). The first stage of conventional PV systems are the PV cells (arranged in single modules, strings or arrays) responsible for the DC power generation, which depends, mostly, on the solar irradiance and temperature. To interface the DC power generated and the AC grid typically, a two-level voltage source inverter (VSI) composed of power electronic devices is employed. The PV inverter is controlled to achieve the grid connection requirements such as synchronization, protection, anti-island detection, etc (Teodorescu; Liserre; Rodriguez, 2007a).

Typically, transformerless inverters are available on the market with power ratings commonly from 1 kW to 8 kW for single-phase products (Canadian Solar, 2021; PHB Solar, 2021; SMA Solar Technology, 2021). A DC-DC conversion stage is usually found in these topologies, due to the interesting features such as the capacity of decoupling the PV system operation point and the PV inverter grid control, boost the PV modules DC voltage if needed, perform maximum power point tracking (MPPT) control and provide galvanic isolation, depending on topology (Teodorescu; Liserre; Rodriguez, 2007a; Abu-Rub;

Malinowski; Al-Haddad, 2014). The design and production of a PV system has as challenge obtaining high efficiency, power quality, low failure rates and low cost (Petrone et al., 2008; Bialasiewicz, 2008).

As the PV system power generation depends on solar irradiance and temperature, intermittent variations in climatic conditions over the day result in fluctuating power delivered to the grid. Moreover, at distribution levels, where PV systems numbers increases substantially, the grids are less robust than transmission grids and, due to the radial configuration, as the voltage level decreases their reliability also tends to decrease (Mastromauro et al., 2009). In view of these facts, several works in literature have been discussing the possibility of using the PV inverters current margin for adding extra functionalities to the PV system to support the electrical grid and increase its hosting capacity (Torquato et al., 2018). Therefore, these multifunctional PV inverters could provide ancillary services, with low additional cost and without exceeding their rated current limits, such as low voltage ride-through, reactive power compensation, frequency support and power quality enhancements related to harmonic mitigation (Acuña et al., 2014; Yang et al., 2016; Xavier; Cupertino; Pereira, 2018).

In this context, the harmonic distortion has been one of the main concerns in several stages of EPS's. Nowadays, this problem has gotten worse with the high penetration of grid-connected nonlinear loads resulting from rectifiers with typical voltage source loads (cell phone chargers, notebooks, etc.). For instance, the increasing utilization of uninterruptible power supplies, personal computers and electronic and entertaining devices has led to a harmonic content proliferation at commercial and residential installations. The growth in high harmonics content circulation over distribution grids reduces the power quality, resulting in higher distribution power losses, thermal effects on transformers, resonance interactions, interference in nearby communication and overheating and pulsating torque in rotation machines (De la Rosa, 2006).

The stiffer the AC grid is, lower will be the voltage distortion across the system. At distribution level, where the grid tends to be less stiff, the harmonic distortions become a more significant problem due to the distortions on the voltage. Fig. 3 illustrates a typical scenario of nonlinear load and distributed generator connected to the grid, through a tie line (R_g and L_g). The DPGS has as main objective the processing of the active power. Therefore, only the fundamental load current is supplied by the DPGS, leaving the entire harmonic current content circulates between the grid and nonlinear load. As results, voltage harmonic distortions may arise at the point of common coupling (PCC) depending on the nonlinear current amount and high feeder impedance in a low-voltage (LV) system, as presented in Fig. 3. Weak grids are defined as a grid with lower short-circuit capacity and they are the worst-case scenario in this context, resulting in high PCC voltage distortion due to the high line impedances. Therefore, standards for harmonic control, such as IEEE

caused by harmonic current circulation across the grid lines are reduced.

The harmonic mitigation functionality for VSI-interfaced DPGS units, which includes PV systems, has been proposed in several works in literature by using voltage- and current-controlled mode converters (VCM and CCM, respectively). Fig. 4 presents a classification and summarization for the HC strategies according to their features and control mode.

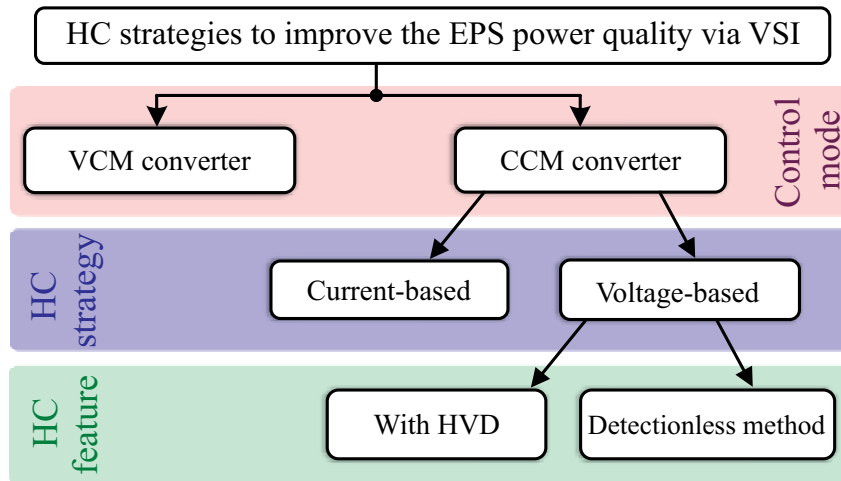


Figure 4 – Overview of strategies proposed in the literature to grid power quality improvements using VSI's.

Since output AC voltage is the controlled quantity, VCM converters are particularly desirable at autonomous islanding operation because of their capability of providing direct voltage and frequency support for the loads (Yunwei Li; Vilathgamuwa; Poh Chiang Loh, 2004; Lee; Cheng, 2007; Wang et al., 2011b; Savaghebi et al., 2015; Mousavi et al., 2017). Besides, as approached in He, Li and Munir (2012), the harmonic voltage compensation through virtual impedance control can be relatively easy to implement in this control mode. However, the harmonic current sharing between converters may be a complex task since each harmonic current order is controlled separately (Zhao et al., 2018a). The VCM converters family has an extensive number of control strategies. However, they will not be the focus of this work due to low application on grid-connected commercial PV systems.

The CCM scheme is the most used when referring to grid-connected converters due to the control capability over the active and reactive power exchange (Teodorescu; Liserre; Rodriguez, 2007a). The HC strategy typically applied to that scheme consists in measuring the load current, through external sensors, and inject the measured current harmonic components in opposite phase (Bojoi et al., 2011; Tang et al., 2012; Zou; Wang; Cheng, 2014; Xavier; Cupertino; Pereira, 2018; Bonaldo; Morales Paredes; Pomilio, 2016). Thereby, the harmonic currents of nonlinear loads are provided by the DPGS units avoiding harmonics circulation through the upstream grid, improving the grid current quality and, hence, indirect improving the PCC voltage, since there is no harmonic voltage drops in

the line impedances. However, this approach requires converters hardware changes and external sensors for nonlinear loads currents measurements, which may be an inconvenience when multiple loads are connected at different points along the grid.

In reality, depending on the distance between the PCC and the converter, current measurements delays may occur, affecting the control design. A different approach using only local measurements are the voltage-based HC strategies proposed in [Akagi \(1997\)](#), [Akagi, Fujita and Wada \(1999\)](#), [Jintakosonwit et al. \(2002\)](#), [Wada, Fujita and Akagi \(2002\)](#) for shunt-APF's and in [Pogaku and Green \(2006\)](#), [He et al. \(2014\)](#), [Li and He \(2014\)](#), [Zhao et al. \(2018b\)](#), [Zhang et al. \(2019\)](#) for DPGS's. The concept of this strategies, independently of the specific features, is based in using the control loops to manipulate the converters output impedance at harmonic frequencies.

Initially, reference [Akagi \(1997\)](#) proposed, for the first time, a voltage-detection-based APF emulating a virtual resistance. The converter output behavior is characterized as a resistor for selective harmonic frequencies, aiming to damp the harmonics propagation throughout a long distribution line. Further on, the same author investigates, in [Jintakosonwit et al. \(2002\)](#), [Wada, Fujita and Akagi \(2002\)](#), the strategy gain design and the evaluation of the whack-a-mole effect in a specific electrical distribution system, respectively. Still in this line, [Li and He \(2014\)](#) discuss the aspects of this strategy for CCM-based DPGS's and highlights that the knowledge of the feeder impedance is required for better HC performance, especially when HC is shared among multiple DPGS's. In [Pogaku and Green \(2006\)](#) several DPGS's with resistive active-power filter (R-APF) functionality are evaluated in a radial distribution line and the harmonic resistance is adapted according to the target total harmonic distortion (THD). More recently, [Nie et al. \(2018\)](#) proposed an enhanced control strategy adjusting the optimal virtual resistor value to meet the load harmonic amplitude requirements and a control loop using the filter capacitor voltage to adjust the harmonic current reference phase.

A different strategy for DPGS's is proposed in [Zhao et al. \(2018b\)](#) called voltage feedback-based harmonic compensator, which uses the PCC harmonic voltage as reference and feedbacks with the filter capacitor voltage to achieve the compensation. However, it assumes an impedance between the converter and the PCC. Thus, extra sensors are required to measure the PCC voltage.

In the strategies discussed so far, an accurate harmonic voltage detector (HVD) is essential for the compensator correct operation ([Asiminoael; Blaabjerg; Hansen, 2007](#)), such as Fourier transform-based detection method ([Chen et al., 2018](#)), second-order generalized integrator (SOGI) ([Rodríguez et al., 2011](#)), conservative power theory (CPT) ([Marafao et al., 2015](#)), delayed-signal-cancellation-based detection ([Wang; Li, 2013](#)) and instantaneous power theory ([Akagi; Kanazawa; Nabae, 1984](#)). The harmonic extraction process increases, considerably, the required converters microcontroller processing time and must be taken

into account during the system design.

On the other hand, the detectionless voltage-based HC methods are an interesting solution for reducing processing time. As example, reference [He et al. \(2014\)](#) proposes a current controller with two parallel control branches, one responsible for fundamental current control and the other for harmonic current control, where the reference could be generated by a virtual resistor technique or local load current measurement. On the same line, the authors of [Zhang et al. \(2019\)](#) propose a voltage compensator aiming to reshape the converter output impedance, providing a low-impedance path for undesirable harmonic content.

Regardless of the HC technique chosen, some aspects must be considered when the HC capability is included in PV inverters. The first point, since several frequencies are present in the controlled signal, the controllers must be able to act and be tuned at these different frequencies. For this purpose, references [Mastromauro et al. \(2009\)](#), [Wu, Panda and Xu \(2010\)](#), [Yepes et al. \(2011\)](#) have addressed resonant and repetitive controllers with high gains adjustments in each interested frequency. Another important point is the detection of the harmonic content required for some techniques for a reliable reference generation, as discussed before. Each one of the detection methods cited so far focuses on different aspects such as: detection accuracy, time response, system stability and selectivity.

Another important point that must be observed is the inverter current capacity. PV inverters have a current limitation defined according to the electronic switching devices for certain design conditions and, if this value is exceeded the devices may be damaged. Thus, a technique for limiting the inverter current is required when HC is performed for ensure a safe operation ([Xavier; Cupertino; Pereira, 2018](#)). Reference [Yang, Wang and Blaabjerg \(2014\)](#) addressed a simpler current peak limitation technique considering only the inverter current fundamental component. However, as several frequencies are present in the inverter current during HC, the current peak calculation and limitation by an analytical expression may be a complex solution.

In fact, different techniques have been proposed in literature to limit the PV inverter injected current peak. Conventional saturation (CS) schemes consist in defining an upper and lower value for the current and have as drawback adding undesirable low order harmonics components into the grid, disrupting the HC technique performance. In order to avoid this problem, dynamic saturation (DS) techniques decrease the compensated harmonic components amplitude according to the PV inverter current availability. In other words, the compensation of harmonics is reduced, focusing in the main service of the PV system, which is active power injection. The DS technique brings the partial HC capability to the PV inverters, permitting harmonic components compensation within their current capacity. Even though, this technique requires an algorithm for monitoring the inverter current and reduce the harmonic current reference when the inverter reach its rated current.

Hence, this algorithm time response, which is expected to be as fast as possible, should be considered during inverter control design.

The authors in reference [Ting Qian et al. \(2005\)](#) approached a closed-loop DS technique applied to shunt active power filters with the objective of calculating a multiplying factor to reduce harmonic reference. However, the work did not present experimental results to validate the technique and system stability analysis. Reference [Pogaku and Green \(2006\)](#) proposed a DS algorithm based on synchronous reference frame for inverter-interfaced distributed generators aiming harmonic mitigation into the grid. Again, no experimental validation is performed and also a deep analysis on the inject current peak is not performed. Further, another closed-loop DS technique for distributed generators is proposed in [Gajanayake et al. \(2009\)](#) using a proportional-integral (PI) controller for current limiting based on a moving window RMS calculator. However, limiting RMS current value in a multiple frequencies signal may not yield satisfactory results, since the current peak could be higher than the RMS value itself, causing possible damages in the inverter. More recently, reference [Xavier et al. \(2019\)](#) propose an open-loop based DS algorithm with the objective of limiting the inverter current peak value during HC with low computational burden and memory requirements. The proposed algorithm calculates in a simple manner the harmonic current amount that can be injected without exceeding the inverter rated current, expressed by a harmonic compensation factor. Besides, the authors present an experimental validation on the technique, which highlights the technique operation in practical conditions. The same reference indicates to future analysis when multiple PV inverters with partial HC capability are connected in a line.

1.1 Objectives, Contributions and Limitations

In view of the aforementioned points, the DS techniques leads to a partial HC in PV inverters. When multiple PV inverters with partial HC capability are connected in a line, the global effects would depend on the individual compensation capacity and on the HC technique employed. Therefore, this work aims to evaluate the partial harmonic compensation in a distribution radial line with multiple PV inverters. Based on the general purpose, the following topics will be approached in this work:

1. *Modeling and control of single-phase double-stage grid-connected PV inverter:* The objective is present a brief discussion about the converter topology and the conventional control strategies employed in these systems;
2. *Current-based and voltage-based harmonic compensation strategies applied to PV inverters:* A description of the main concepts for two different harmonic compensation strategies are presented in this topic. A simplified analytical modelling is performed to investigate the techniques;

3. *Dynamic saturation strategy*: This topic discusses the operation of the dynamic current saturation algorithm employed at this work.

Regarding the topics mentioned above, the work presents the following contributions:

- *Implementation and study of the partial harmonic compensation applied to multiple PV systems using a dynamic saturation algorithm;*
- *Methodology to adjust the compensation gain for a voltage-based harmonic compensation strategy;*
- *Comparison between a current-based and a voltage-based harmonic compensation strategy applied to PV inverters in a case study system;*

The real electrical power lines have different and complex configurations. The proposed case study aims to investigate a simplified radial line. For bigger or different line configurations, a study needs to be carried out for each case.

1.2 Text Organization

This work is organized in five chapters. Chapter 1 has presented the context, motivation, objectives, contributions and limitations of the present work. Chapter 2 presents the theoretical basis about PV inverters structure, conventional control strategies and harmonic compensation strategies. Chapter 3 presents the proposed case study system. Chapter 4 presents the simulation results for evaluation and comparison of the harmonic compensation strategies applied to the case study system. Finally, conclusions and futures developments of this work are stated in Chapter 5.

1.3 Related Publication

A published paper derived from this project is given as follows:

1. A. L. P. de Oliveira, L. S. Xavier, J. M. S. Callegari, A. F. Cupertino, V. F. Mendes and H. A. Pereira, "Partial Harmonic Current Compensation Applied to Multiple Photovoltaic Inverters in a Radial Distribution Line," 2019 IEEE 15th Brazilian Power Electronics Conference and 5th IEEE Southern Power Electronics Conference (COBEP/SPEC), Santos, Brazil, 2019, pp. 1-6.

2 Methodology

This chapter presents a description of the fundamental concepts of single-phase double-stage PV systems. An overview of the system topology and the most common control strategies are presented. Then, the harmonic compensation strategies based on load current measurement and based on local voltage measurement are discussed, as well as the dynamic saturation strategy, which is necessary for including the HC capability on the system.

2.1 Single-Phase Double-Stage PV Systems

Fig. 5 shows the schematic for a two-stage single-phase grid-connected PV system. The first stage is composed by the DC/DC boost converter, in which the PV arrays are connected in the input. The solar cells are the base element responsible for solar photovoltaic conversion and, since the solar cells presents low power generation (from 1 W to 2 W, typically), for practical applications this cells are associated in series or/and parallel to form the PV modules. Further, the PV modules are also associated to form structures with higher power capability, the PV arrays (Rauschenbach, 1980). The PV arrays model can be represented by a direct current source in parallel with a diode and equivalent series and parallel resistances. Villalva, Gazoli and Filho (2009) proposed a method for modelling the PV arrays characteristics using informations present in most PV arrays datasheets, which describes the cell output current as a function of its constructive features, solar irradiance and operational temperature. This mathematical model for PV arrays is used for the following case study simulations due to the simplicity of obtaining the model parameters.

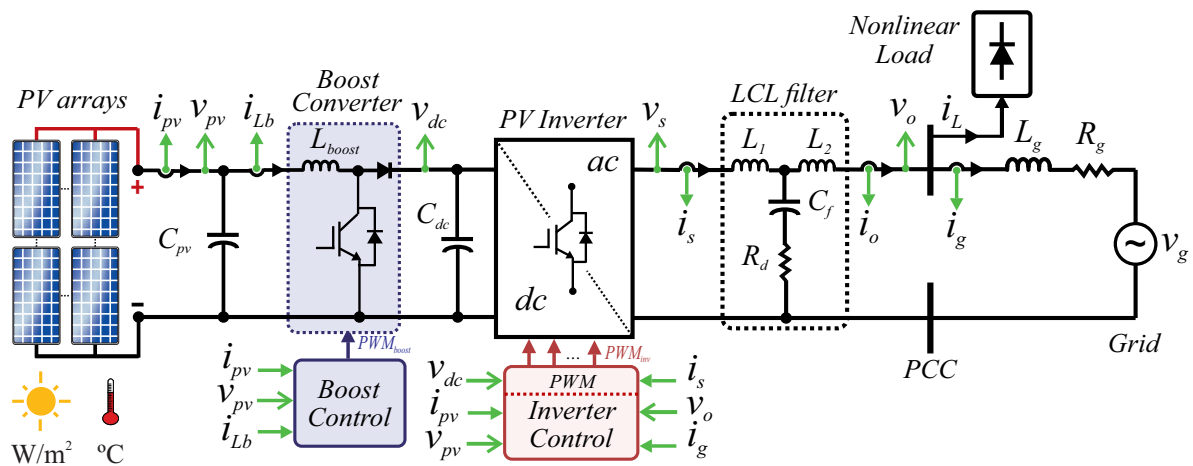


Figure 5 – Schematic of a two-stage single-phase grid-connected PV system.

Since the PV modules power generation depends on ambient conditions, a MPPT algorithm should be implemented to ensure the maximum power extraction from the modules. The Perturb and Observe (P&O) is one of the most traditional MPPT algorithms. A specific implementation for the (P&O) is called incremental conductance method is used in this work, which consists in the evaluation of the incremental conductance (di/dv) in each interaction (Esrām; Chapman, 2007).

In distribution grid-connected applications, the range of inverters input voltage is, generally, between 200 V and 800 V. The DC/DC stage converter is used, typically, to boost the PV arrays voltage in order to maintain an admissible voltage level required for startup the system and extending the operation range during low solar irradiance conditions. Besides, for single-phase applications, the MPPT algorithm implementation within the DC/DC stage control allows increasing efficiency and reduce voltage fluctuations on DC-link capacitor for PV systems integration (Blaabjerg et al., 2006b; Yang; Zhou; Blaabjerg, 2017). Thus, for single-phase PV systems with a DC boost stage connected to a line with 220 V (line-to-line), the DC-link voltage is usually adjusted around 400 V (Yang, 2014). Fig. 6(a) shows the boost control diagram implemented with a MPPT algorithm and two control loops based on proportional-integral (PI) controllers, as reported in Xavier (2018).

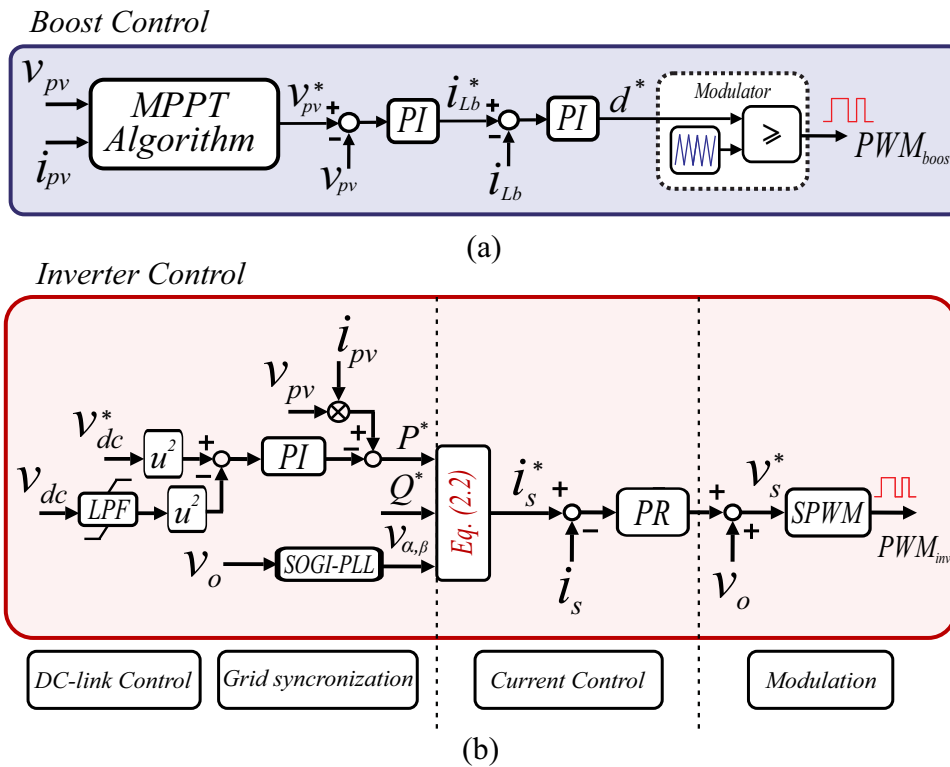


Figure 6 – (a) Boost converter control block diagram. (b) Inverter fundamental control block diagram.

The second stage consists on a full-bridge DC/AC voltage source inverter which

interfaces the DC power delivered by the PV arrays and the AC electrical grid. All the power extracted by the boost converter must be transferred to the grid. This requirement is achieved by controlling the DC-link voltage in a level that ensures the power flow. Moreover, the PV inverters connection to the PCC with the grid is, in general, made by a passive filter, aiming to reduce high harmonic components resulting from the switching process. The LCL filters is a suitable topology for this purpose, since it offers a lower inductors volume, better cost and higher attenuation at high switching frequencies. However, LCL filters inserts resonance issues in the power system and requires a careful design. [Gomes, Cupertino and Pereira \(2018\)](#) presents an overview of damping techniques for grid-connected voltage source converters based on LCL filters which can be used to reduce resonances effects. A resistor inserted in series to filter capacitor is a simple solution for passive resonance damping, but it has as disadvantage reduction on PV inverter efficiency.

The inverter fundamental control block diagram is shown in Fig. 6(b). This control strategy is composed by an outer loop responsible for controlling the DC-link voltage, which results in controlling the injected active power, and an inner loop designed to control the inverter output current. In this context, a synchronization between the PV inverter and the utility grid is essential for a suitable operation. In fact, monitoring grid variables is an indispensable task for grid-connected converters, since several eventualities could affect power systems ([Teodorescu; Liserre; Rodriguez, 2007b](#)). In single-phase inverters the synchronization task is widely performed by Phase-Locked Loop (PLL) algorithms. In this work, the PLL method proposed in [Ciobotaru, Teodorescu and Blaabjerg \(2006\)](#) is adopted. The proposed structure associates a SOGI and a synchronous reference-frame PLL (SRF-PLL). The SOGI structure generates filtered quadrature signals in $\alpha\beta$ -reference frame, v_α and v_β , that are transformed to dq -reference frame to perform the grid angle tracking using the SRF-PLL. This PLL structure offers a simple implementation and a good performance under distorted voltage grid conditions.

Furthermore, the modulation level is required to determine the switching power devices states, ensuring the average synthesized inverter output voltage. The most common modulation technique for single-phase voltage source grid-connected applications is the pulse width modulation (PWM). In particular, the unipolar sinusoidal PWM (SPWM) strategy is an appropriate choice for this work, resulting in a three level output voltage and the allocation of high-frequency spectrum, inherent to the modulation process, to double of switching frequency ([Holmes; Lipo, 2003; Amorim et al., 2018](#)).

In general, the single-phase PV system control must be designed to meet the interconnection requirements according to the guidelines of [IEC \(2004\)](#). In the cascaded control approach, shown in Fig. 6(b), the outer loop provides the current reference for the inner loop, which generates the reference voltage for the modulator. This scheme requires a higher bandwidth for inner loop controller than for outer loop to ensure control stability.

In other words, the inner loop response must be sufficiently faster than the outer loop response.

The current controller employed for the inner loop is a proportional-resonant (PR) controller which provides a high gain at the resonant frequency and reduces the steady state error, resulting in zero error tracking to the fundamental current reference (i_α^*) (Yepes, 2011). The PR controller transfer function is given by:

$$G_{PR}(s) = K_p + K_{r,f} \frac{s}{s^2 + \omega_f^2}, \quad (2.1)$$

where K_p is the proportional gain, $K_{r,f}$ is the resonant gain at fundamental frequency and ω_f is the fundamental angular frequency. While K_p affects directly the transient response speed through bandwidth regulation, $K_{r,f}$ can be adjusted to offer a trade-off between selective filtering and dynamic response. Indeed, Yepes (2011) presents guidelines for PR-controller design and highlights that the effects on stability can be disregarded for high $K_{r,f}$ values. The guidelines in Yepes (2011) are used in PR-controllers design herein. In addition, a feedforward action for the grid voltage (v_o) is inserted at the current controller output in order to reduce the controller effort.

The outer loop controls the DC-link voltage, as previously discussed. For this purpose the method based on v_{dc}^2 control is employed, as approached in Yazdani and Iravani (2010). For control design purposes, the inner and outer loops can be considered decoupled due to the time response difference. A first order low-pass filter (LPF) with cut-off frequency adjusted in a quarter of the fundamental frequency is used for the DC-link voltage measurement, avoiding control performance degradation (Buso; Mattavelli, 2015). The v_{dc}^2 control strategy uses a PI controller to calculate the active power to be injected to the grid in order to keep the power balance on DC-link capacitor. Besides, the PV power generated (P_{pv}) is added to the control to reduce controller efforts. Moreover, it is important to include an anti wind-up action in the PI controller to prevent an integral controller deep saturation during transients (Buso; Mattavelli, 2015).

According to PQ-theory, the current references in $\alpha\beta$ -reference frame can be found by using the active power reference (P^*) produced by DC-link voltage control loop and the reactive power reference (Q^*) as follows (Yang, 2014):

$$i_\alpha^* = \frac{2}{v_\alpha^2 + v_\beta^2} (v_\alpha P^* + v_\beta Q^*), \quad (2.2)$$

where v_α and v_β are the grid voltage at fundamental frequency in stationary reference frame provided by the SOGI structure. The Q^* is set to zero since ancillary services related to reactive power are not included in this work.

2.2 Harmonic Compensation Strategies

The discussion about HC capability is carried out analysing Fig. 7. Firstly, harmonic components are added to inverter current reference, when harmonic current compensation is performed. Thus, a resonant controller must be designed aiming to track the compensated harmonic components, resulting in a proportional multi-resonant controller (PMR) (Yepes, 2011). Accordingly, the transfer function for the PMR controller is given by:

$$G_c(s) = K_p + \sum_{h=1}^n K_{r,h} \frac{s}{s^2 + (h\omega_h)^2}, \quad (2.3)$$

where K_p is the same proportional gain present in (2.1), $K_{r,h}$ are the resonant gains for the harmonic orders $h = 1, 2, 3, \dots, n$ and ω_h is the angular resonance frequency.

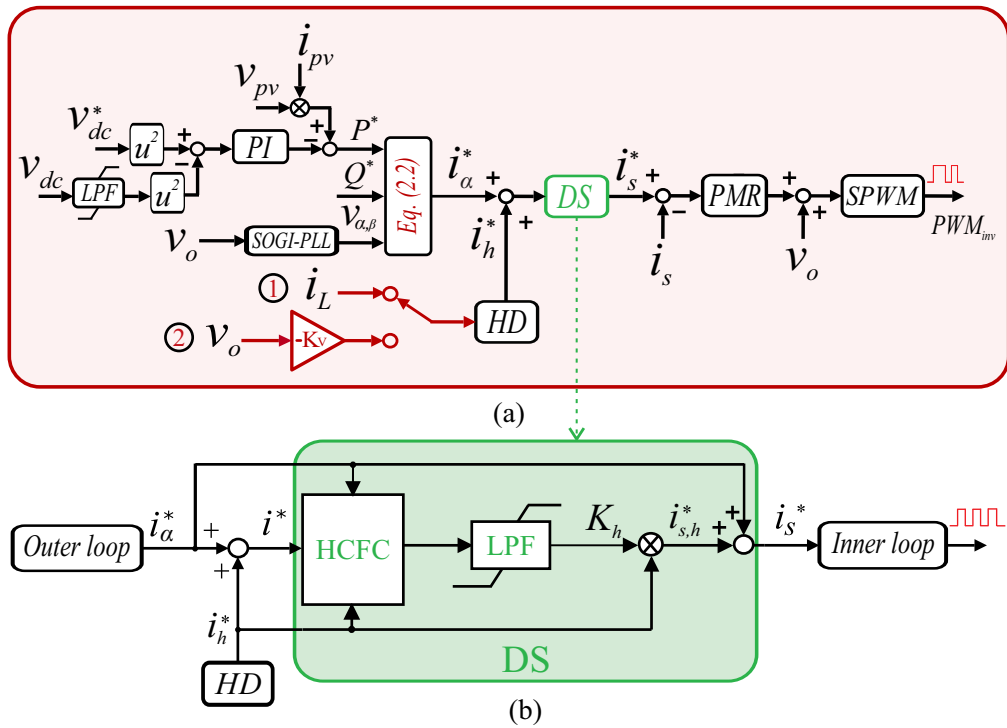


Figure 7 – (a) Inverter with HC capability control block diagram. (b) Dynamic saturation block diagram.

Secondly, the harmonic detection (HD) block is responsible to extract the harmonic components from the input harmonic reference signal (signals (1) and (2) on Fig. 7(a)). In this work a infinite-impulse response (IIR) bandpass filter associated in cascade with a notch filter is used for this purpose. The HD transfer function is given by:

$$H_d(s) = F_{NT}(s)F_{BP}(s), \quad (2.4)$$

$$F_{NT}(s) = \frac{s^2 + \omega_f^2}{s^2 + s\omega_b + \omega_f^2} \text{ and } F_{BP}(s) = \frac{s(\omega_{c1} - \omega_{c2})h}{s^2 + s(\omega_{c1} - \omega_{c2})h + (\omega_{c1} - \omega_{c2})^2h^2} \quad (2.5)$$

where ω_f is the fundamental angular frequency, ω_b is the notch filter bandwidth, ω_{c1} the lower band cut-off frequency, ω_{c2} the upper band cut-off frequency and h the harmonic order. Basically, the filter is adjusted to have an unitary gain at the selected harmonic frequencies and attenuate the other frequencies, especially the fundamental frequency where the notch filter is adjusted (Shynk, 1989; Williams; Taylor, 1995; Tang et al., 1996).

Foward, the harmonic current reference (i_h^*) is added to fundamental current reference (i_α^*). This resulting signal is sent to the dynamic saturation (DS) block to verify the harmonic amount that can be compensated without exceeding the inverter current limit. More details about the DS algorithm is discussed in the next sections.

2.2.1 Conventional Harmonic Compensation Strategy

In the conventional HC strategy, represented by the signal from switch (1) in Fig. 7(a), the PV inverter works cancelling the harmonic current from local nonlinear loads. Thus, the harmonic content circulates between the arms of the PV inverter and the local nonlinear loads. This requirement is achieved by measuring the nonlinear load current (i_L), extracting its harmonics components and injecting a proportional harmonic current in counter-phase. Thus, the nonlinear load harmonic current which used to be supplied by the utility grid is fully or partially provided by the PV system (Li; He, 2014).

In fact, depending on the number of nonlinear loads connected at the same PCC, the current measurement of each load becomes impractical. Commonly, for this strategy, the grid current (i_g) and the inverter current (i_s) are measured to obtain the i_L information. Nevertheless, measuring i_g may not be an easy task. Depending on the distance between the PCC and the PV inverter measurement delays may occur, affecting the compensation performance, which should be considered in the control design. Savaghebi et al. (2012) approaches a measuring system that requires a low-bandwidth communication channel link to exchange data packages of harmonic magnitude and phase.

For analytical modelling purposes, the PV system is simplified as shown in Fig. 8 and the following assumptions are made (Zhang, 2019):

- *The switching-frequency harmonics are ignored when modeling the frequency response of the VSI output voltage (v_s) to the set-point of the PWM (v_s^*): the switching frequency (f_{sw}) for the VSI full-bridge topology is normally higher than the compensated grid harmonic frequencies;*

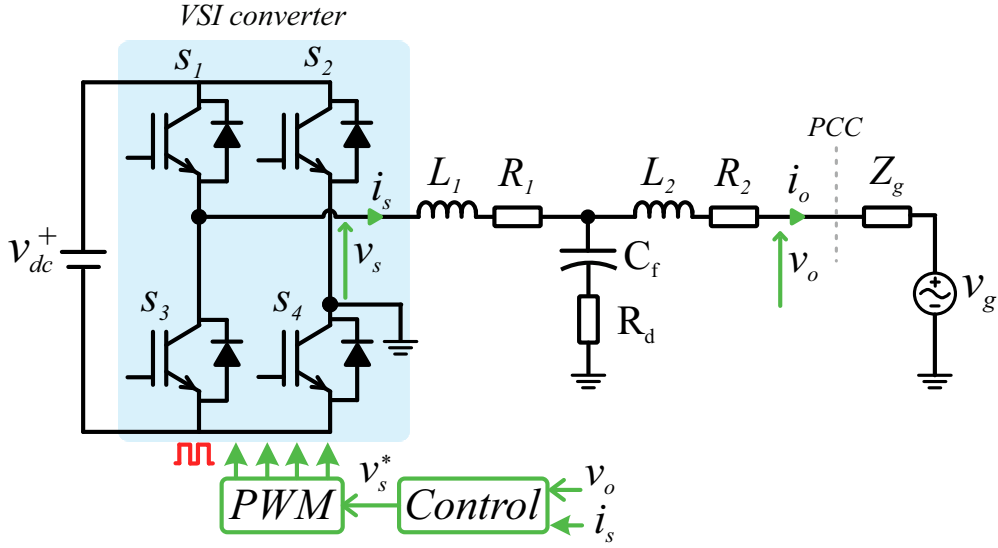


Figure 8 – Simplified PV system for modelling purposes.

- *The DC voltage supply is constant:* This assumption is valid for steady state conditions with the outer loop well regulated;
- *The PLL output is decoupled from the PCC voltage:* The PLL algorithm is designed to be insensitive to disturbances from the PCC voltage and, therefore, time invariant for modeling purposes;
- *The nonlinear load current measured is static and independent of the PCC voltage:* This assumption gives that the current reference is decoupled from the PCC voltage.
- *The effects of DS algorithm are disregarded for simplicity.*

Therefore, a linear average model can be developed as:

$$v_s(s) = v_s^*(s)H(s), \text{ with } H(s) = e^{-sT_d}. \quad (2.6)$$

where T_d is a delay that depends on the PWM scheme implementation and the switching frequency (Corradini et al., 2015). For sampling period (T_s) equal to the inverter switching period (T_{sw}) and SPWM unipolar scheme, the value of T_d is $1.5T_s$ (Hoffmann et al., 2016). In simulation platform and for modelling purpose, $H(s)$ can be expressed by a second order padé approximation as (Xing; Ploeg; Nijmeijer, 2016):

$$H(s) = e^{-sT_d} \approx \frac{12 - 6T_d \times s + T_d^2 \times s^2}{12 + 6T_d \times s + T_d^2 \times s^2}. \quad (2.7)$$

Further, assuming that the filters components are linear, the converter side output current (i_s) related to the PCC voltage (v_o) and the PWM set-point is given by:

$$i_s(s) = \frac{H(s)}{Z_{th}(s)}v_s^*(s) + \frac{-k(s)}{Z_{th}(s)}v_o(s), \quad (2.8)$$

with,

$$k(s) = \frac{Z_c(s)}{Z_2(s) + Z_c(s)}, \text{ and } Z_{th}(s) = \frac{Z_2(s)Z_c(s)}{Z_2(s) + Z_c(s)} + Z_1(s). \quad (2.9)$$

Above, Z_1 , Z_2 and Z_c are the impedances of converter-side inductor, grid-side inductor and filter capacitor branch, respectively. Equations (2.8) and (2.9) represent the open-loop model for the grid-connected VSI. The open-loop system is susceptible to grid low-order harmonics disturbances and is expected that the fundamental output current would not be in phase with the PCC voltage. The control algorithm is applied to solve this issues.

Following the assumptions aforementioned, the control strategy gives:

$$v_s^*(s) = (i_s^*(s) - i_s(s))G_c(s), \quad (2.10)$$

where, $i_s^*(s)$ is the generalized inverter current reference and $G_c(s)$ is the current controller transfer function presented at (2.3). Applying (2.10) to (2.8), the closed-loop model is given by:

$$i_s(s) = k_{cl}(s)i_s^*(s) - \frac{1}{Z_{cl}(s)}v_o(s), \quad (2.11)$$

with,

$$k_{cl}(s) = \frac{H(s)G_c(s)}{H(s)G_c(s) + Z_{th}(s)}, \text{ and } \frac{1}{Z_{cl}(s)} = \frac{k(s)}{H(s)G_c(s) + Z_{th}(s)}. \quad (2.12)$$

Therefore, the converter with the conventional closed-loop control can be represented by an equivalent Norton circuit, as shown in Fig. 9(a). The bode diagram with fundamental frequency of 60 Hz in Fig. 9(b) and Fig. 9(c) represent the frequency response for the transfer functions $k_{cl}(s)$ and $1/Z_{cl}(s)$, respectively. High magnitude gains are typically designed for the grid fundamental and the harmonic frequencies in $G_c(s)$ with the objective of maintain a good reference tracking performance. As shown by the frequency response, the conventional HC strategy has the characteristic of high output impedance for both fundamental and harmonic frequencies, while the current references gain ($k_{cl}(s)$) is expected to be unitary, to maintain the control performance. It is noteworthy that the current

reference is composed by the converter fundamental current and the nonlinear loads measured current.

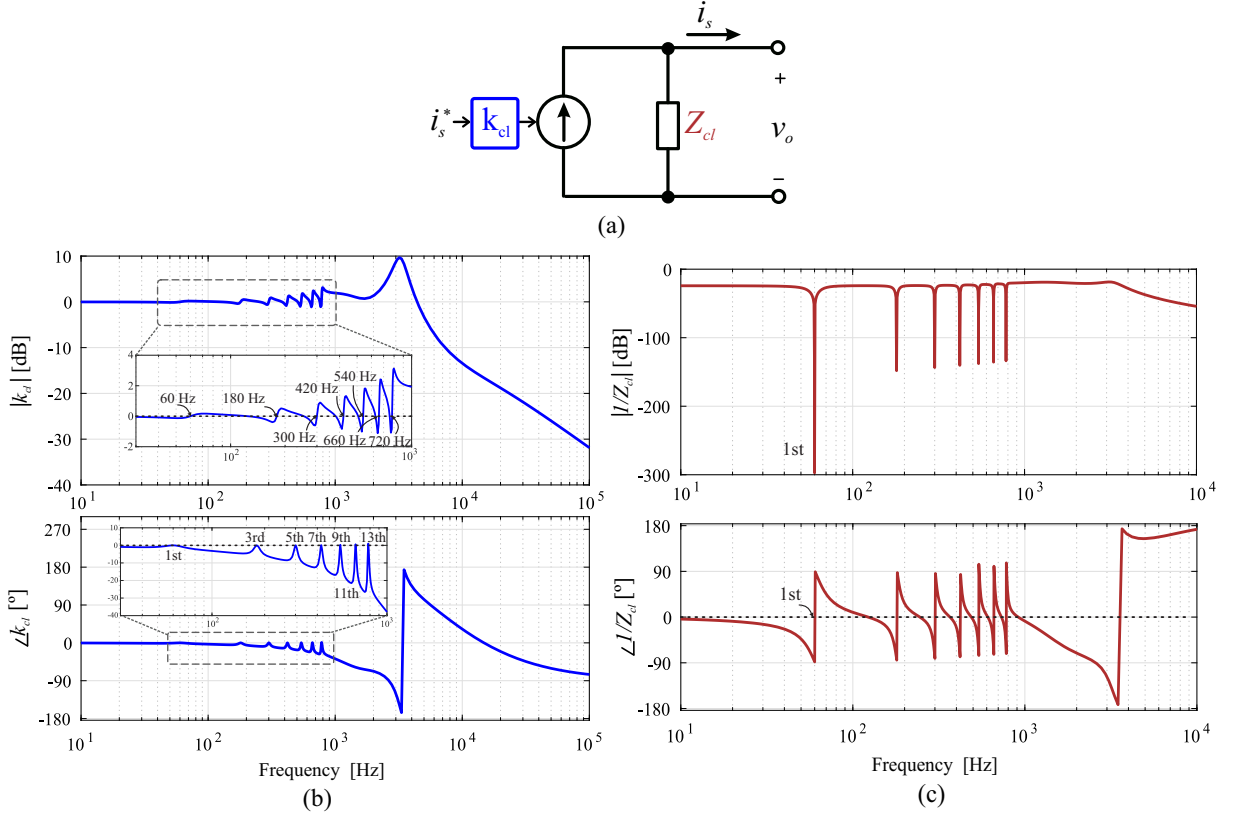


Figure 9 – Conventional HC strategy: (a) Equivalent circuit closed-loop representation. (b) Bode plot of the transfer function $k_{cl}(s)$. (c) Bode plot of the transfer function $1/Z_{cl}(s)$.

2.2.2 Local Voltage-Based Harmonic Compensation Strategy

The first local voltage-based HC strategy was proposed in Akagi (1997) for CCM APFs, with the objective to emulate a resistor at selective harmonic frequencies and, thus, to damp the harmonic content circulation in distribution systems. Subsequent works studied the APF installation site, power electronic converters topology, experimental results, the whack-a-mole effect and automatic gain adjustment by means of the voltage THD (Akagi; Fujita; Wada, 1999; Jintakosonwit et al., 2002; Wada; Fujita; Akagi, 2002).

The same concept can be applied to DPGS's with CCM. The basic idea is to direct the nonlinear load current to the DPGS side in order to maintain only the sinusoidal fundamental current flow into the grid. The reference signal (2) from the switch in Fig. 7(a) represents this HC strategy. The current reference for this virtual harmonic resistance control is given by:

$$i_s^*(s) = i_\alpha^*(s) + i_{h(s)}^* = i_\alpha^*(s) - H_D(s)v_o(s)K_v, \quad (2.13)$$

where K_v is the compensation gain, which can be interpreted as the inverse of the virtual resistor and $H_D(s)$ is the transfer function of the harmonic detector.

In this control scheme, the voltage in the DPGS point of connection (PoC) is measured. The nonlinear load harmonic current passes through the feeder impedance, between the PoC and the PCC with the grid, and causes distortions in the PoC voltage (a distinction between the definition of PoC and PCC can be found in [IEEE... \(2018\)](#)). The virtual resistor emulated by the HC control strategy makes a harmonic current with the same phase of the distorted voltage circulate into the inverter. However, since the feeder impedance is modelled as an inductor and a resistor, at least phase errors are expected when the local voltage-base HC is employed ([He; Li; Munir, 2012; Lee; Li; Cheng, 2009](#)). Particularly for sharing the harmonic compensation among multiple DPGS, its important to note that for high feeder impedance, the information about the PCC voltage and the feeder impedance is desired in order to perform accurate harmonic compensation ([Li; He, 2014](#)). For the analytical modelling the PoC and PCC voltages are assumed as equals, in other words, is assumed that there is no impedance between the PCC and the PoC. Furthermore, the compensation gain (K_v) should be adjusted according HC requirements, inverter available current and system stability range.

The linear average model for this control scheme follows the same assumptions aforementioned except that the harmonic current reference has a direct relation with the PCC voltage. Basically, the same process can be applied until the equations (2.11) and (2.12). Then, replacing $i_s^*(s)$ by the relation in (2.13), results in:

$$i_s(s) = k_{cl}(s)i_\alpha^*(s) - \left(\frac{1}{Z_{cl}(s)} + \frac{1}{Z_h(s)} \right) v_o(s), \quad (2.14)$$

with,

$$\frac{1}{Z_h(s)} = \frac{K_v H_D(s) H(s) G_c(s)}{H(s) G_c(s) + Z_{th}(s)}. \quad (2.15)$$

In this form, it is noted that the local voltage-based HC strategy inserts a parallel impedance $Z_h(s)$ at the output impedance. Thus, the system closed-loop operation can be represented by the equivalent circuit in Fig. 10(a), where the gain transfer function $k_{cl}(s)$ and output impedance $Z_{cl}(s)$ frequency responses have already been shown at Fig. 9(b) and Fig. 9(c), respectively.

Fig. 10 (b) shows the frequency response for the transfer function $1/Z_h(s)$ with a fundamental frequency of 60 Hz and a K_v gain equals 1. It should be observed that the transfer function has higher gains at the harmonic frequencies selected in the HD algorithm. Besides, the transfer function phase is close to 0° , which indicates that the transfer function acts essentially as a resistance at the selective harmonic frequencies.

Further, Fig. 10 (c) shows a zoomed view in the dashed area of Fig. 10 (b) to highlight the system operation. In the same figure, the compensation gain K_v is varied to observe the transfer function behavior. It is noticed that while the transfer function magnitude increases as the gain increases, the phase remains constant, indicating only a change in the resistance value.

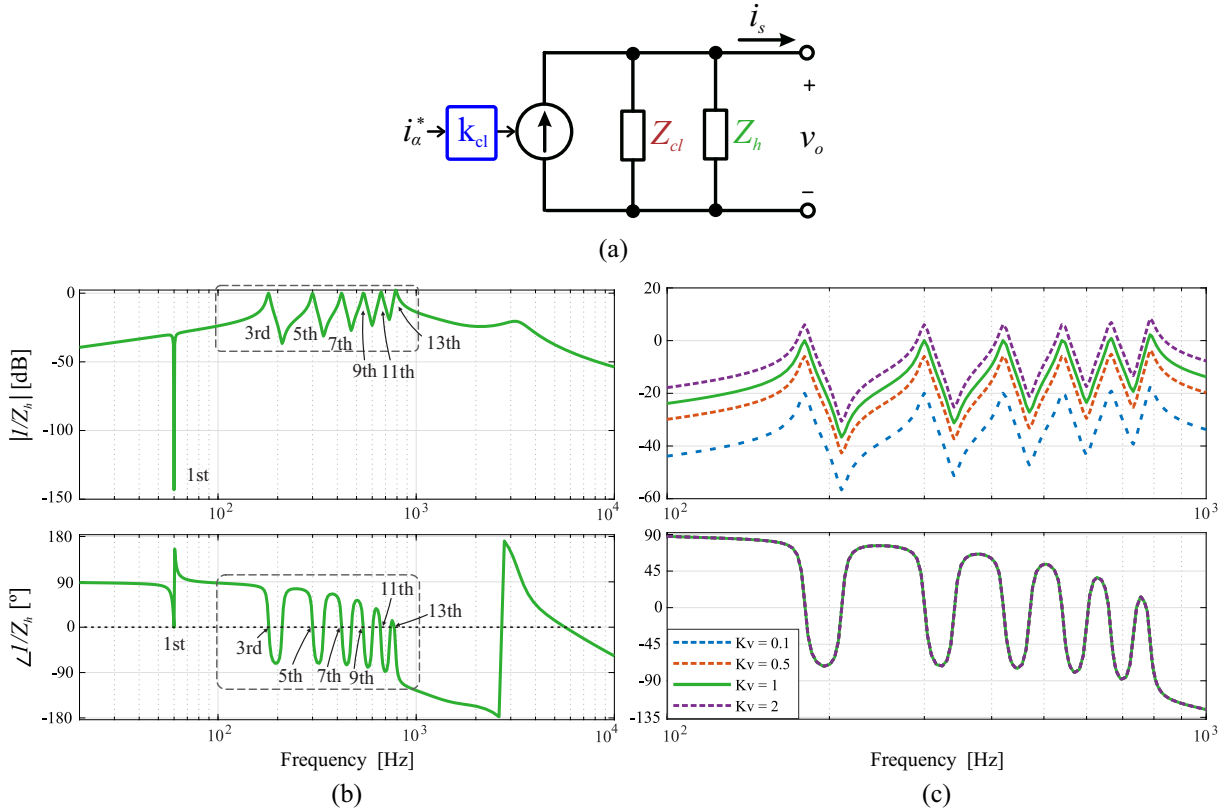


Figure 10 – Local voltage-based HC strategy: (a) Equivalent circuit closed-loop representation, (b) Bode plot of the transfer function $1/Z_h(s)$, (c) Zoomed view of the bode plot $1/Z_h(s)$.

2.2.3 Impedance-based Stability Analysis

In order to provide an accurate harmonic compensation, a stable operation should be ensured when connecting the closed-loop system to the grid. As shown in Fig. 8, the upstream grid is represented by its Thévenin circuit, where Z_g is the equivalent impedance and v_g is the voltage supply seen at the PCC (Zhang, 2019). The PV system can be represented by the closed-loop equivalent circuit for the HC schemes presented in the previous sections. The relation between the PCC voltage and the grid voltage can be found as:

$$v_o(s) = i_s(s)G_1(s) + v_g(s)G_2(s), \quad (2.16)$$

where,

$$G_1(s) = \frac{Z_c(s) \cdot Z_g(s)}{Z_2(s) + Z_c(s) + Z_g(s)}, \text{ and } G_2(s) = \frac{Z_2(s) + Z_c(s)}{Z_2(s) + Z_c(s) + Z_g(s)}. \quad (2.17)$$

For the *conventional HC strategy*, replacing (2.16) in (2.11) gives:

$$i_s(s) = i_s^*(s) \underbrace{\frac{k_{cl}(s) \cdot Z_{cl}(s)}{Z_{cl}(s) + G_1(s)}}_{G_{i,1}(s)} - v_g(s) \underbrace{\frac{G_2(s)}{Z_{cl}(s) + G_1(s)}}_{G_{v,1}(s)}. \quad (2.18)$$

This transfer functions represent a direct relation between the inverter output current, the PV system and grid parameters. It is noteworthy that a transfer function represented by the summation or multiplication of two others transfer functions is stable, if the two sub-transfer functions are stable (Zhang, 2019). Therefore, the stability of transfer functions $G_{i,1}(s)$ and $G_{v,1}(s)$ can be assumed by evaluating their sub-transfer functions. Since $v_g(s)$ and $Z_g(s)$ have no unstable poles, the grid can be assumed stable under open-loop and short-circuit conditions. The LCL filter design assuming the inductors resistance and the damping resistor in series with the capacitor ensures a stable condition for the filter elements impedance. Further, the inverter current reference $i_s^*(s)$, following a regulated outer loop the conventional PLL design, is assumed time invariant and, consequently, stable. Finally, the adopted current controller $G_c(s)$ design also contains no unstable poles. In conclusion, the conventional HC strategy with the correct design does not lead to unstable operations over grid parameters changes.

Similarly, for the *local voltage-based HC strategy*, replacing (2.16) in (2.14) gives:

$$i_s(s) = i_s^*(s) \underbrace{\frac{k_{cl}(s) \cdot Z_{eq}(s)}{Z_{eq}(s) + G_1(s)}}_{G_{i,2}(s)} - v_g(s) \underbrace{\frac{G_2(s)}{Z_{eq}(s) + G_1(s)}}_{G_{v,2}(s)}, \quad (2.19)$$

where $Z_{eq}(s)$ represents the equivalent output impedance for this strategy, given by the parallel association between $Z_{cl}(s)$ and $Z_h(s)$, whose poles location depends on the value of K_v .

In general, the stability analysis for the transfer functions $G_{i,2}$ and $G_{v,2}$ follows the same concepts as the previous analyzed transfer functions $G_{i,1}$ and $G_{v,1}$. However, the transfer functions of (2.19) have a new degree of freedom inserted by the virtual resistor loop, which directly affects the system stability. In fact, by analyzing the poles on transfer functions $G_{i,2}$ and $G_{v,2}$ is possible to determine a stable operation range for the compensation gain K_v according to grid impedance Z_g variations. For low-voltage distribution power lines (distribution lines are typically short), the impedance is mainly represented by a inductor (L_g) and a resistor (R_g). Besides, the ratio X/R value, which

represents the relation between the line reactance and the line resistance, is typically assumed smaller than one (Liserre; Teodorescu; Blaabjerg, 2006).

Fig. 11 shows the stability limit curve for the local voltage-based HC strategy using the parameters described on chapter 3. In this case study a ratio X/R equals 0.8 is assumed. Fig. 11 (a) shows the stability limit curve which presents the higher gain K_v that can be employed without lead the system to instability, in the range of the grid inductance from 0.1 mH to 10 mH. Moreover, Fig. 11 (b) shows the transfer functions $G_{i,2}$ and $G_{v,2}$ poles variation with the gain K_v for L_g equals 1 mH. Further, Fig. 11 (c) presents a zoomed view on the area where the poles crosses between the stable and unstable region. This results will be used to choose the gain K_v in the following case study chapter.

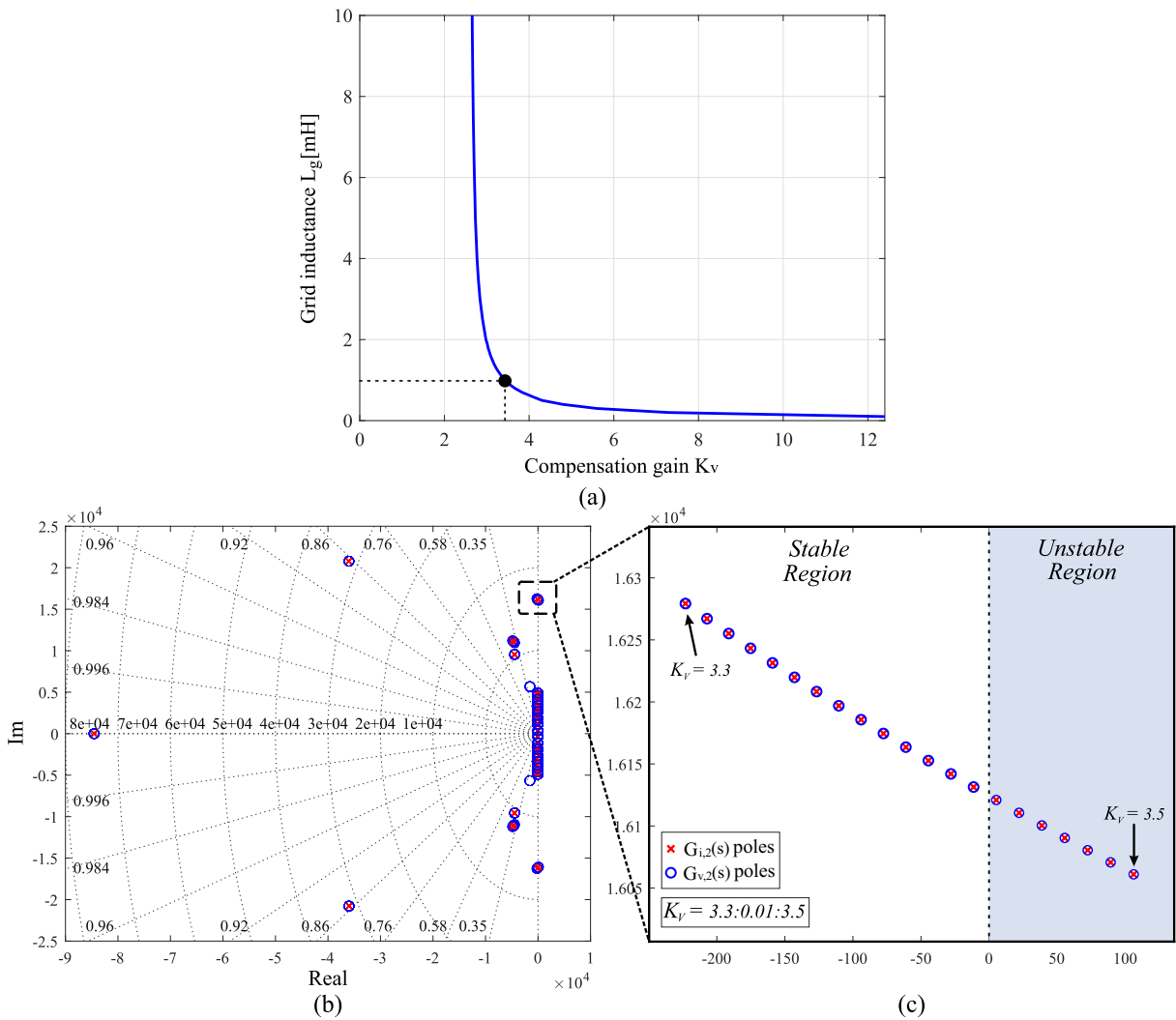


Figure 11 – Local voltage-based HC strategy stability analysis. (a) Stability limit curve. (b) Closed-loop transfer functions poles. (c) Zoomed view on the stable region limit.

It is noteworthy that new analysis should be performed for different grid conditions. A brief procedure for tuning the K_v gain is described in the following, for typical parameters of single-phase grid-connected PV inverters and distribution grids:

- Define a grid line inductance L_g range and a X/R ratio;
- For the first grid impedance value defined in the previous topic, compute the transfer functions $G_{i,2}$ and $G_{v,2}$ for a K_v variation from 0 to 20;
- Construct the poles and zeros diagram for the previous transfer functions and verify the K_v value at which at least one of the transfer functions become unstable. In other words, when the transfer functions poles pass to the right half-plane of the plan S;
- If no instability is found for this K_v range, increase its range and repeat the previous procedures;
- Save the ordered pair (L_g, K_v) just before instability;
- Repeat the second, third and fourth topics for the remaining L_g values;
- Construct the stability limit graphic, as in the Fig. 11 (a);
- Define the K_v value based on the constructed stability limit graphic and according to the case study interest.

2.3 Dynamic Saturation Scheme

Fig. 12 shows a comparison between CS and DS techniques time and frequency performances. Since the CS technique cuts the current waveform in the limit values, the square form resulting in the current peaks inserts extra harmonics in the inverter output current. On the other hand, the DS technique overcome this limitation and ensures a better harmonic performance by reducing the compensated harmonic components and maintaining the fundamental component in order to keep the PV inverter output current within its capacity, introducing the partial HC capability.

The DS scheme approached at this work is proposed by the authors in [Xavier et al. \(2019\)](#), which the block diagram is shown in Fig. 7(b). The proposed DS technique is based on a open-loop algorithm with the fundamental current reference i_α^* , harmonic current reference i_h^* and inverter total current reference i^* as inputs. The harmonic compensation factor calculation (HCFC) algorithm is responsible to calculate the factor K_h by analysing the contribution value of i_α^* and i_h^* to the peak value of i^* . Thus, K_h ensures a safety harmonic current injection without exceeding the inverter rated current I_m^* . The step-by-step operation is described as follows:

- Verify, at each sampling, if the i^* value is increasing. If it increased, store this value as well as the i_α^* and i_h^* contributions to this value.

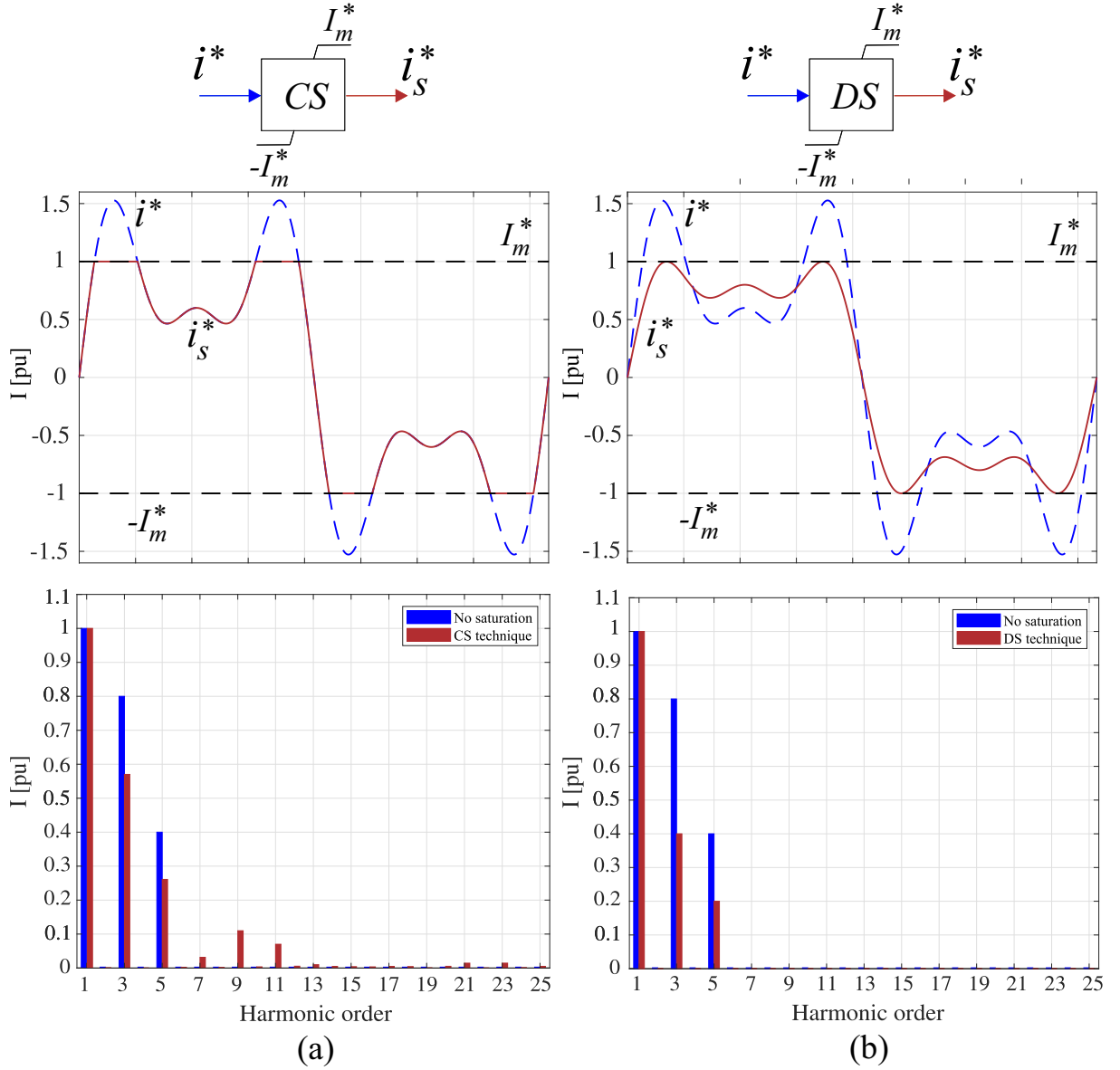


Figure 12 – Inverter reference current waveform and the injected current spectrum. (a) Conventional saturation. (b) Dynamic saturation.

- Passing a fundamental frequency cycle of analysis, the peak value of i^* is stored in I_m and i_α^* and i_h^* contributions are stored in I_h and I_α , respectively.
- A decision is made by comparing I_m and I_m^* , which can be obtained through the datasheet. If $I_m \leq I_m^*$, the K_h is adjusted to 1, allowing the total HC. Generally, this condition is always satisfied if $I_h < 0$. On the other hand, the $I_m > I_m^*$ condition implies that there is no current margin to perform total HC. The factor K_h is automatically set to zero if $I_\alpha \geq I_m^*$, disabling HC capability. Otherwise, the partial

HC is provided by means of the following equation:

$$K_h = \frac{I_m^* - I_\alpha}{I_h}. \quad (2.20)$$

Since HCFC is a real-time operating algorithm, it is subject to abrupt variations. To overcome this drawback, a LPF, saturated in 0 and 1, is added at the algorithm output to suppress possible oscillations. Besides, a delay of a fundamental frequency cycle is insert in the K_h calculation and the LPF cutoff frequency is designed to be a quarter of the fundamental frequency component. Thereby, the new harmonic current reference ($i_{s,h}^*$) that will be sent to control is represented as:

$$i_{s,h}^* = K_h \underbrace{\sum_{h=1}^m I_h \cos(\omega_h t + \phi_h)}_{i_h^*}. \quad (2.21)$$

Thus, the new inverter current reference (i_s^*) is given by this new harmonic current reference added to the fundamental current component (i_α^*). This DS structure is valid for both HC strategies, since both provides a current as the harmonic reference for compensation purposes. In fact, for the local voltage-based HC strategy the effect of the factor K_h is cascade associated with the compensation gain K_v , which can be interpreted as changing the virtual resistor value.

2.4 Chapter Closure

This chapter presented the description of a two-stage single-phase PV system. The main system elements were discussed as well as the the traditional control loop strategies. Focusing mainly on the DC/AC stage, the inverter control structure was discussed for a fundamental current control, including grid synchronization algorithms, DC-link voltage control and the sinusoidal PWM modulation strategy. The requirements to include the harmonic compensation capability to the PV inverter were also discussed, which involves changing the current controller, the harmonic detection method and the dynamic saturation algorithm. Two harmonic compensation strategies were depicted. The conventional control strategy consists in measuring the local loads current and the local voltage-based strategy uses only the PCC voltage measurement. For both techniques an analytical simplified model was discussed and also an impedance-based stability analysis was presented aiming to ensure the system stable operation.

3 Partial HC Applied to Multiple PV Inverters: a Case Study

This chapter applies the concepts discussed so far in a case study system. Selective partial harmonic compensation according to the idle power capacity of PV systems is addressed into a low-voltage three-phase radial distribution grid. The line loads and impedances are based on a typical real urban system. The parameters of the single-phase grid-connected PV systems distributed over the line are also discussed. Finally, it is assumed that distributed generators with the harmonic compensation capability are sufficiently spaced to experience different solar irradiance conditions on the respective PV arrays surface.

3.1 Case Study System Description

The adopted low-voltage three-phase distribution power system structure is shown in Fig. 13. It is a radial system, where the medium voltage three-phase upstream grid supplies the power line through a delta-star transformer with 75 kVA apparent power rating and a transform ratio of 13.8:0.22 kV. The analyzed structure covers only a branch of the power lines connected to this transformer. There are five nodes in the power line with different unbalance electrical passive loads connected to each one. The loads parameters can be found in the Table 1.

Table 1 – Parameters of the three-phase star-connected (Y) and single-phase loads.

Load	Phase a		Phase b		Phase c	
	R_a [Ω]	L_a [mH]	R_b [Ω]	L_b [mH]	R_c [Ω]	L_c [mH]
1	5.56	5.90	9.68	8.56	9.68	8.56
2	-	-	13.90	14.75	-	-
3	5.56	5.90	9.68	8.56	9.68	8.56
4	4.74	7.55	12.90	17.11	4.74	7.55
5	13.90	14.75	13.90	14.75	13.90	14.75

Further, the Table 2 shows the grid impedance values and the distribution impedance values. The line/transformer impedance values refer to the impedance between two consecutive nodes in the line and the distribution impedance value refers to the impedance between a certain node and the PV system point of connection. This last impedance values is varied to evaluate the effects on the partial HC capability.

Three single-phase PV systems are two-phases connected at nodes 3, 4 and 5. For instance, the PV system 1 is connected to the phases *C* and *A*, the PV system 2 to the

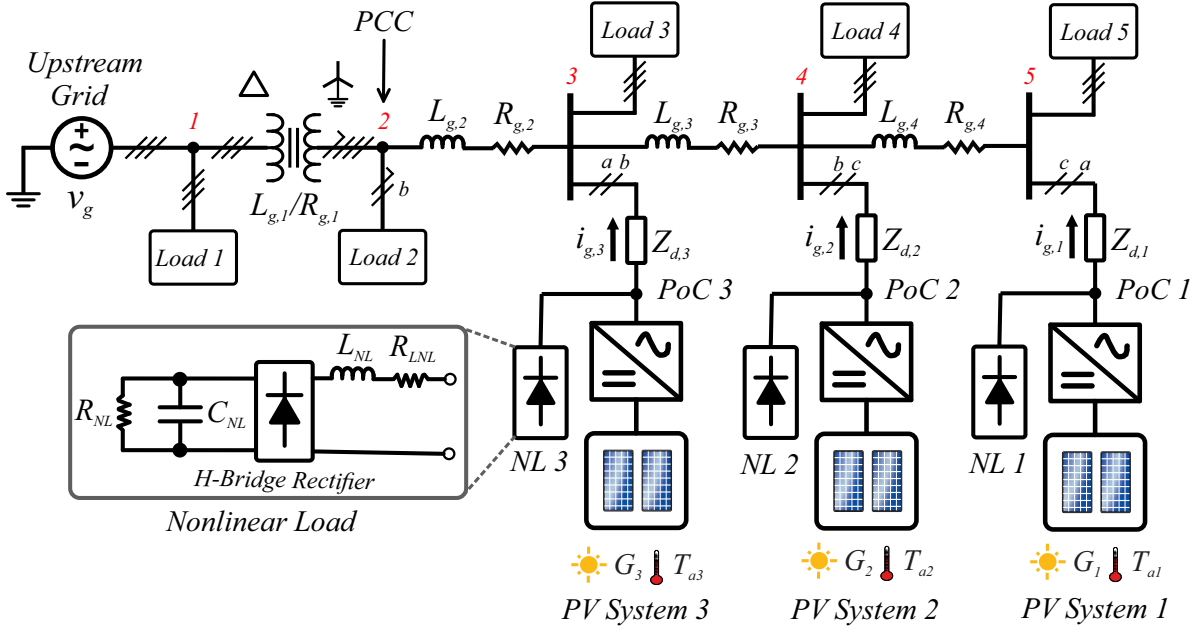


Figure 13 – Single-phase grid-connected PV systems into the case study radial distribution line.

Table 2 – Distribution line impedance values.

Parameter	Label	Value
Transformer impedance 1	$L_{g,1}/R_{g,1}$	31.6 μ H/32 m Ω
Line impedance 2	$L_{g,2}/R_{g,2}$	19.98 μ H/20.6 m Ω
Line impedance 3	$L_{g,3}/R_{g,3}$	36.7 μ H/37.8 m Ω
Line impedance 4	$L_{g,4}/R_{g,4}$	36.7 μ H/37.8 m Ω
Distribution impedance 1	$L_{d,1}/R_{d,1}$	0.1-2 mH/ X/0.8 Ω
Distribution impedance 2	$L_{d,2}/R_{d,2}$	0.1-2 mH/ X/0.8 Ω
Distribution impedance 3	$L_{d,3}/R_{d,3}$	0.1-2 mH/ X/0.8 Ω

phases B and C and the PV system 3 to the phases A and B . As highlighted in the Fig. 13, there is nonlinear loads at the same point of connection of the PV systems, which are represented by a single-phase H-bridge diode rectifier. Therefore, the harmonic current circulates between two line phases and interactions between the harmonic contents of the nonlinear loads connected in a same phase are expected. Moreover, different voltage distortions appears across the line caused by the harmonic current circulation through the feeder impedances.

The case study aims to evaluate the harmonic compensation demanded by the local nonlinear load, using PV inverters idle current margin. Each PV system has different power ratings and consequently different current limits. Furthermore, the PV systems are subjected to different ambient conditions. Thereby, the harmonic current that flows to the upstream grid is the remaining current that the PV systems were unable to compensate. Note that there is no communication link between the PV systems and each one performs

its own local measurements for HC purposes.

The PV systems and nonlinear loads parameters are shown in Table 3. Besides, the nonlinear load current spectrum is shown in Fig. 14. Table 4 shows the parameters of a 250 W traditional commercial PV module employed for the PV arrays of this work. Among the evaluated converters, the inverter 3 has higher power rating. Besides, for the sake of simplicity and computational efforts reduction, the PV strings are connected in parallel with the same boost converter in this work.

Table 3 – Parameters of the multiple single-phase PV inverters and nonlinear loads connected into the radial line.

Parameters	Inverter 1	Inverter 2	Inverter 3
Grid voltage - line to line (v_g)	220 V	220 V	220 V
Inverter: switching frequency (f_{sw})	18 kHz	18 kHz	18 kHz
Inverter: sampling frequency (f_s)	18 kHz	18 kHz	18 kHz
Inverter: fundamental frequency (f_n)	60 Hz	60 Hz	60 Hz
DC-link voltage (v_{dc})	400 V	400 V	400 V
PV array rated power (P_{max})	4 kW	3 kW	6 kW
PV array configuration (N_s, N_p)	(8,2)	(6,2)	(8,3)
Inverter rated power (S_{max})	4 kVA	3 kVA	8 kVA
Peak inverter current (I_{max})	27.0 A	20.2 A	51.3 A
LCL filter inductance (L_1/L_2)	1/0.45 mH	1/0.45 mH	1/0.45 mH
LCL filter capacitance (C_f)	20 μ F	20 μ F	20 μ F
LCL filter damping resistor (R_d)	4 Ω	4 Ω	4 Ω
LCL filter inductance X/R ratio	20	20	20
dc-link capacitance (C_{dc})	3 mF	3 mF	3 mF
Boost: inductance (L_{boost})	0.8 mH	0.8 mH	0.8 mH
Boost: inductor resistance (r_b)	10 m Ω	10 m Ω	10 m Ω
Boost: capacitance (C_{pv})	0.5 mF	0.5 mF	0.5 mF
Boost: switching frequency (f_{swb})	18 kHz	18 kHz	18 kHz
NL load: inductor (L_{NL})	1 mH	1 mH	1 mH
NL load: inductor resistance (R_{LNL})	0.06 m Ω	0.06 m Ω	0.06 m Ω
NL load: capacitor (C_{NL})	2 mF	2 mF	2 mF
NL load: resistor (R_{NL})	150 Ω	150 Ω	150 Ω

3.2 Case Study Configurations

The case study system is implemented in the software PLECS by a discrete simulation. Ideal switching devices are employed since system losses and efficiency are not discussed herein. The inverter control is designed using the sampling frequency (f_s) equal to the switching frequency and the simulation fixed step size is adjusted to $f_s/128$. The PI controller are discretized by the Foward Euler method, while the resonant controllers are discretized by the Tustin with Prewarping method to ensure the resonance peak at the correct frequency (Yepes, 2011). The controllers parameters are presented in Table 5.

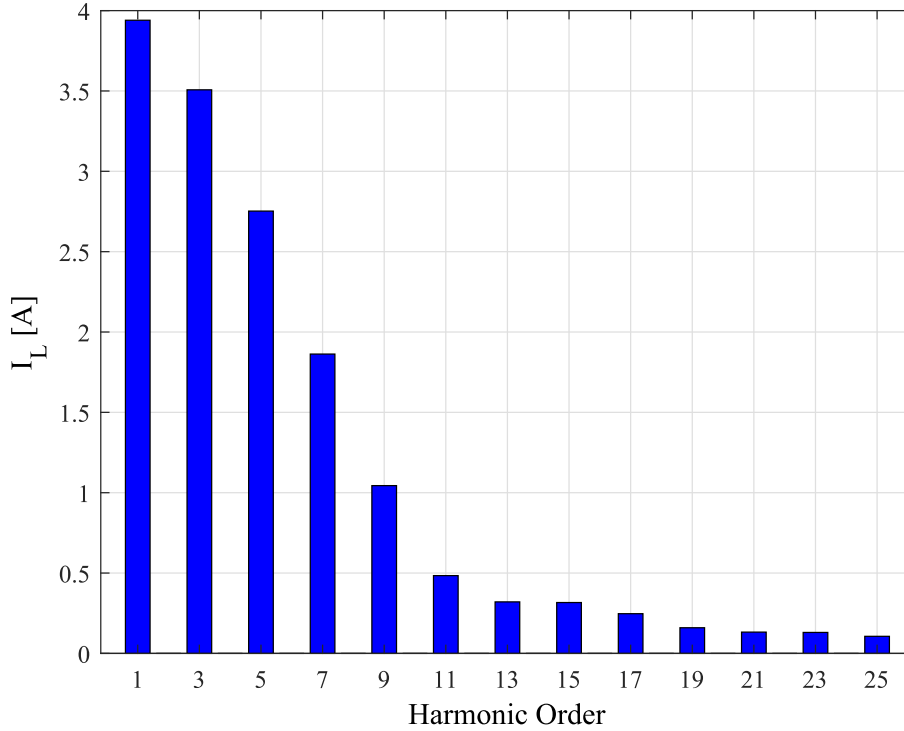


Figure 14 – Current spectra of the nonlinear load used in the case study.

Table 4 – PV module parameters.

Parameter	Value
Maximum power (P_{mpp})	250 W
Open-circuit voltage (v_{oc})	37.5 V
Short-circuit current (i_{sc})	8.5 A
Voltage at maximum power point (v_{mpp})	31.29 V
Current at maximum power point (i_{mpp})	7.99 A
Temperature coefficient of v_{oc} (C_v)	-0.313 %/°C
Temperature coefficient of i_{sc} (C_i)	0.0043 %/°C
Number of cells in series (n_s)	60
Nominal irradiance (G_n)	1000 W/m ²
Nominal operation temperature (T_n)	320 K
Panel series resistance (R_s)	0.173900 Ω
Panel parallel resistance (R_p)	379.023365 Ω

For the boost converter, the inner loop crossover frequency is adjusted to one tenth of the actuator maximum frequency, i.e., one tenth of the boost converter switching frequency (f_{swb}). Further, the outer loop is tuned one tenth below the inner loop operation frequency to ensure decoupling between loops and stability of cascading control. The MPPT algorithm is regulated with a response speed slower than the outer loop for the same reason. The frequency adopted for the MPPT algorithm is 5 Hz.

In the inverter control inner loop, the current controller gains are designed as suggested in the methodology section, considering the HC for the odd harmonic frequencies

Table 5 – Parameters of the controllers for the single-phase PV systems.

Parameter	Inverter 1, 2 and 3
Inverter outer loop: Proportional gain	0.207 Ω^{-1}
Inverter outer loop: Integral gain	2.369 Ω^{-1}/s
Inverter inner loop: Proportional gain	16.130 Ω
Inverter inner loop: Fundamental resonant gain	2000 Ω/s
Inverter inner loop: Harmonics resonant gain	1000 Ω/s
Boost outer loop: Proportional gain	1.131 Ω^{-1}
Boost outer loop: Integral gain	148.812/198.416/223.218 Ω^{-1}/s
Boost inner loop: Proportional gain	0.0226 A^{-1}
Boost inner loop: Integral gain	0.2827 A^{-1}/s
PLL: Proportional gain	76.454 V^{-1}/s
PLL: Integral gain	5684.892 V^{-1}/s^2

up to the 13th order. The DC-link voltage control loop has two poles that are allocated in one tenth and one hundredth below the inner loop bandwidth, respectively (Xavier, 2018). The LCL filter resonance frequency (f_{res}) is set to 3 kHz in a way that it does not influence the harmonic compensation performance.

Once the controllers and PV system parameters are defined, the impedance-based stability analysis can be applied to evaluate the HC strategies under feeder impedance changes. For the local voltage-based HC strategy, the compensation gain K_v has a direct influence in system stability. Thus, by using the stability limit curve obtained by varying the feeder impedance, the K_v gain can be adjusted without bringing instability to the system with local voltage-based HC capability. However, in practical applications, to obtain the exact feeder impedance is not an easy task. In fact, several works in literature research on this subject (Robert et al., 1997; Asiminoaei et al., 2005; Timbus et al., 2006; Ciobotaru et al., 2007; Timbus; Teodorescu; Rodriguez, 2007). Still, the grid impedance estimation topic is outside the scope of this work.

Thereby, in order to be able to apply the local voltage-base HC strategy over different grids, the gain K_v is adjusted to the minimum value in the range analyzed, i.e., the K_v value is set to 2.66, which is the value obtained for the weaker grid condition with L_g equals 10 mH.

In order to evaluate the case study system, three different solar irradiance profile are applied into the PV systems, as shown in Fig. 15. The inverter input power variation allows a distribution of harmonic current compensation between the converters according to their available current margins. The two HC strategies addressed at this work are applied to this case study system with the same parameters for fair performance comparison. The total demand distortion (TDD) is used as figure of merit for evaluate the system currents and the total harmonic distortion (THD) is used for the system voltages. The equations

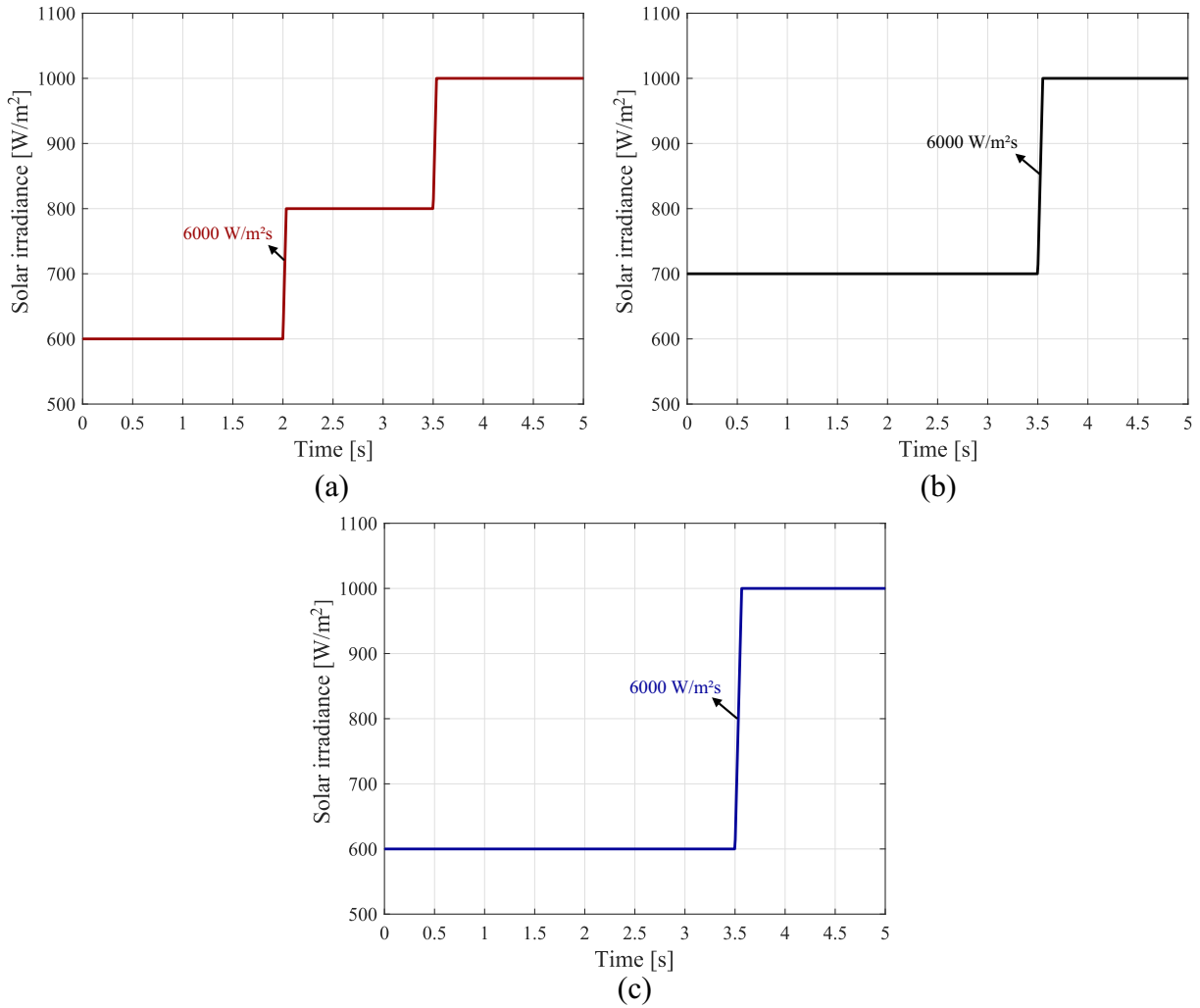


Figure 15 – Case study solar irradiance profile on PV arrays connected to the (a) inverter 1, (b) inverter 2, (c) inverter 3.

for these figure of merit are given by, respectively:

$$TDD = \frac{\sqrt{\sum_{h=2}^n I_{x,h}^2}}{I_{max}} \times 100\%, \quad (3.1)$$

$$THD = \frac{\sqrt{\sum_{h=2}^n V_{x,h}^2}}{V_{x,1}} \times 100\%, \quad (3.2)$$

where $I_{x,h}$ is the x node harmonic component of the analyzed current, I_{max} is the maximum demand current, $V_{x,h}$ is the x node harmonic component of the analyzed voltage, $V_{x,1}$ is the fundamental component of the analyzed voltage and $h = 2, 3, \dots, n$ is the harmonic order. The harmonic components up to the 50th order, excluding interharmonics, are considered as suggested by the Std. IEEE-519 (IEEE..., 2014). The currents and voltages at the PoC between the PV system and the distribution line are chosen to be analyzed, as well

as the currents and voltages at the PCC (node 2, which is the main interconnection point between the upstream grid and the distribution line).

3.3 Chapter Closure

In this chapter, the case study system for evaluating harmonic compensation strategies in a low-voltage distribution line is described. The grid impedance and the loads connected to the line values are presented. Further, the PV system parameters are also presented, as well as the parameters of the PV module employed in the studies. A discrete switching simulation is performed to evaluate the system behavior during different operation conditions and the TDD and THD are used as figure of merit for evaluation. In the next chapter, the simulation results for the two HC strategies are presented and discussed.

4 Results and Discussion

This chapter focuses on the simulation results evaluation for the single-phase PV inverters with HC capability connected into a three-phase low-voltage distribution radial line. Firstly, the HC strategies effects are evaluated for PV systems with current margin to compensate all the harmonic current reference through different grid impedance values. Secondly, the solar irradiance profiles are applied to the PV systems to evaluate their dynamic saturation capability for the two different HC strategies.

4.1 Harmonic Compensation Strategies Evaluation

The first point to be evaluate are the HC strategies steady state effects on the PCC and the PoC of each PV inverter. The figures of merit evaluated are the TDD of the per-phase currents at the PCC (i_{pcc}), the THD of the PCC voltages (v_{pcc}), the TDD of the current that flows to the grid on the PoC ($i_{g,x}$) and the THD of the PoC voltages ($v_{o,x}$), where $x \in \{1, 2, 3\}$ represents one of the three points of connection. The TDD for the PCC currents are calculated with the maximum demand current for the system without distributed generators, which are 77.42 A for the phase *A*, 58.57 A for the phase *B* and 65.51 A for the phase *C*. Meanwhile, the TDD for the PoC currents are calculated with the maximum demand current of the corresponding PV inverter, which were presented in the previous chapter.

The same ambient conditions are configured for both analyzed HC strategies. A constant low solar irradiance profile of 500 W/m² and a constant temperature of 25 °C are adjusted in a way that all PV inverters have current margin for full harmonic compensation. Further, for each HC scheme two grid conditions are analyzed by changing the distribution impedances ($Z_{d,1}$, $Z_{d,2}$ and $Z_{d,3}$) with the same values. The first case evaluated correspond to a weak grid condition by setting the distribution inductances to 2 mH and the resistances are automatically adjusted by the X/R ratio equals 0.8 (typical value of distribution grids).

Fig. 16 shows the results for the described conditions. Fig. 16 (a) shows the TDD of the currents and THD of the voltages before and after the local current-based HC be enabled. A remarkable improvement occurs in the TDD for the PCC and PoC currents. In such weak grid condition, the TDD of the PCC currents decreased from 5.33%, 6.87% and 6.13% to 1.82%, 2.42% and 2.06% for phases *A*, *B* and *C*, respectively. A reduction of 65.91%, 64.77% and 66.39% in the currents TDD values for the phases *A*, *B* and *C*, respectively.

Its noteworthy that the PoC currents have higher TDD values since the maximum

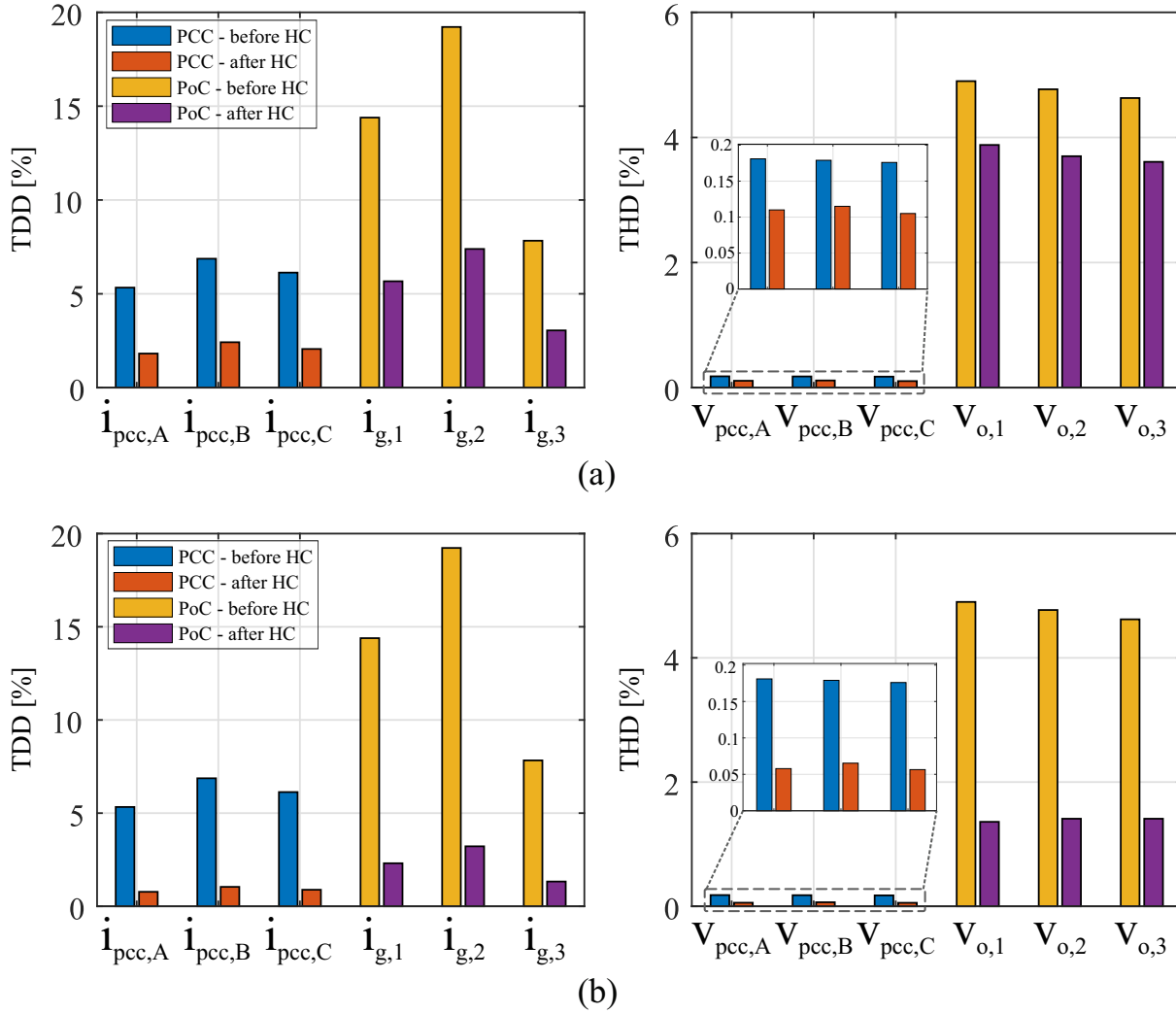


Figure 16 – Weak grid HC strategies evaluation: (a) Local current-based HC scheme. (b) Local voltage-based HC scheme.

demand current of the inverters is lower than the maximum demand current for the whole system. For instance, the TDD for the current in the PoC of PV systems 1, 2 and 3 decreased from 14.39% to 5.67%, 19.22% to 7.39% and 7.83% to 3.05%. At the same time, the improvements in the THD of the voltages are more modest. The reduction on the THD for the PCC voltages in phases A , B and C are 39.23%, 35.75%, 40.34%, respectively. It is observed that similarly to the currents, the harmonic distortions on the PoC voltages are more evident than on the PCC.

Fig. 16 (b) shows the currents TDD and the voltages THD before and after the local voltage-based HC be enabled. In such weak grid condition, the TDD of the PCC currents decreased from 5.33%, 6.87% and 6.13% to 0.78%, 1.04% and 0.89% for phases A , B and C , respectively. Noticeably the improvements for both TDD of currents and THD of voltages are better in this case than the previous one. In fact, the PCC currents TDD are reduced by 85.42%, 84.82% and 85.51% for the phases A , B and C , respectively. In

this same sequence of phases, the PCC voltages THD are reduced by 68.03%, 63.51% and 67.91%.

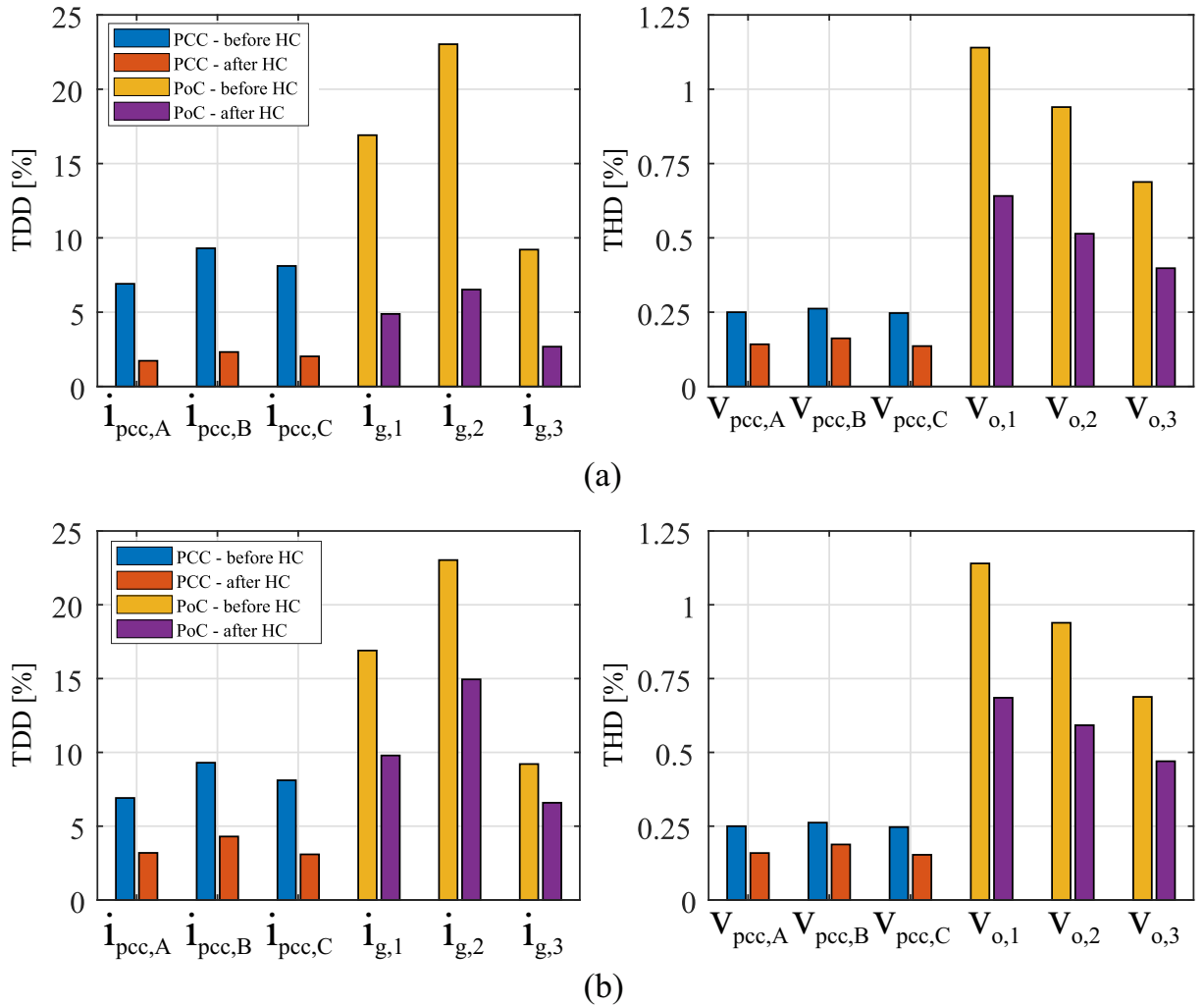


Figure 17 – Stiff grid HC strategies evaluation: (a) Local current-based HC scheme. (b) Local voltage-based HC scheme.

The second case evaluates both HC strategies for a stiffer grid condition with the distribution inductances of 0.1 mH and the resistances adjusted by the X/R ratio. Fig. 17 (a) shows the results for the local current-based HC strategy and Fig. 17 (b) shows the results for the local voltage-based HC strategy. A comparative analysis shows that the local current-based HC strategy reduces the TDD of the PCC per-phase currents in 74.96%, 75.05% and 75.02% for the phases *A*, *B* and *C*, respectively. Also, the reductions for local voltage-based HC strategy are 53.84%, 53.76% and 61.90%. For the PCC voltages THD the differences are smaller, reducing in 43.20%, 38.17% and 44.94% when the local current-based HC strategy is applied and 36.40%, 28.24% and 38.06% for the local voltage-based HC strategy, with the sequence of phases *A*, *B* and *C*, respectively.

Unlike the previous analyzed grid condition the local current-based HC scheme shows better improvements, especially in terms of the PCC currents TDD. These are

expected results since that for stiffer grids the voltages harmonic distortions are less evident. This fact is elucidated by comparing the PoC voltages THD values for the two different grid conditions.

4.2 Case Study System Dynamic Evaluation

Once the HC strategies were evaluated in terms of harmonic distortions reduction, the next point is to evaluate the PV systems dynamic responses when the HC strategies with the DS algorithm are applied over different solar irradiance conditions. The solar irradiance profiles used in this study are shown in the previous chapter. In all of the following analyzes, the ambient temperature is set constant at 25 °C, considering that the analyzed time period is small for significant changes on ambient temperature. Since one HC strategy have proved better than the other for the different analyzed grid conditions, in this study the distribution inductances are set to a middle-term, 1 mH.

4.2.1 Local Current-based HC Strategy Evaluation

Initially, Fig. 18 shows the results for the local current-based HC strategy in terms of the PCC variables. In 0.5 s, the HC is started and the inverters 1 and 3 have current margin to compensate all the harmonic current ($K_h = 1$), while the inverter 2 has a slightly smaller margin with $K_{h,1}$ equals 0.94. At this instant, the PCC currents TDD reduces from 5.97%, 7.89% and 6.97% to 1.73%, 2.36% and 2.14% for phases *A*, *B* and *C*, respectively. It is noteworthy that the TDD of the PCC per-phase currents remain all below 5% after enabling the current-based HC strategy, as suggested by the IEEE Std. 519-2014. Consequently, the PCC voltages THD reduces as a result of reducing the harmonic current propagation at this point. The enlarged view of Fig. 18 (d) shows that the PCC currents waveforms in this moment are distorted. Then, after enabling the current-based HC strategy, they present a behaviour closer to harmonic-free sinusoidal.

In 2 s, the PV system 1 solar irradiance increase to 800 W/m², causing a slightly reduction on its compensation factor $K_{h,1}$ to 0.93. Since the reduction is small, the harmonic compensation remains almost unchanged and the variation on PCC currents TDD and PCC voltages THD is almost imperceptible. Moreover, the increase on solar irradiance increases the fundamental current injected by the inverter 1. Thus, the grid fundamental current supply decreases, as observed on PCC currents waveforms for the phases *A* and *C* shown in the zoomed view Fig. 18 (d).

Further, in 3.5 s the solar irradiance in all PV systems increase to the value of 1000 W/m². At this moment, the PV power generation increases and in order to maintain the output current within the current limits, the harmonic current compensation must be reduced. Therefore, the compensation factor for the inverters 1 and 2 are reduced to

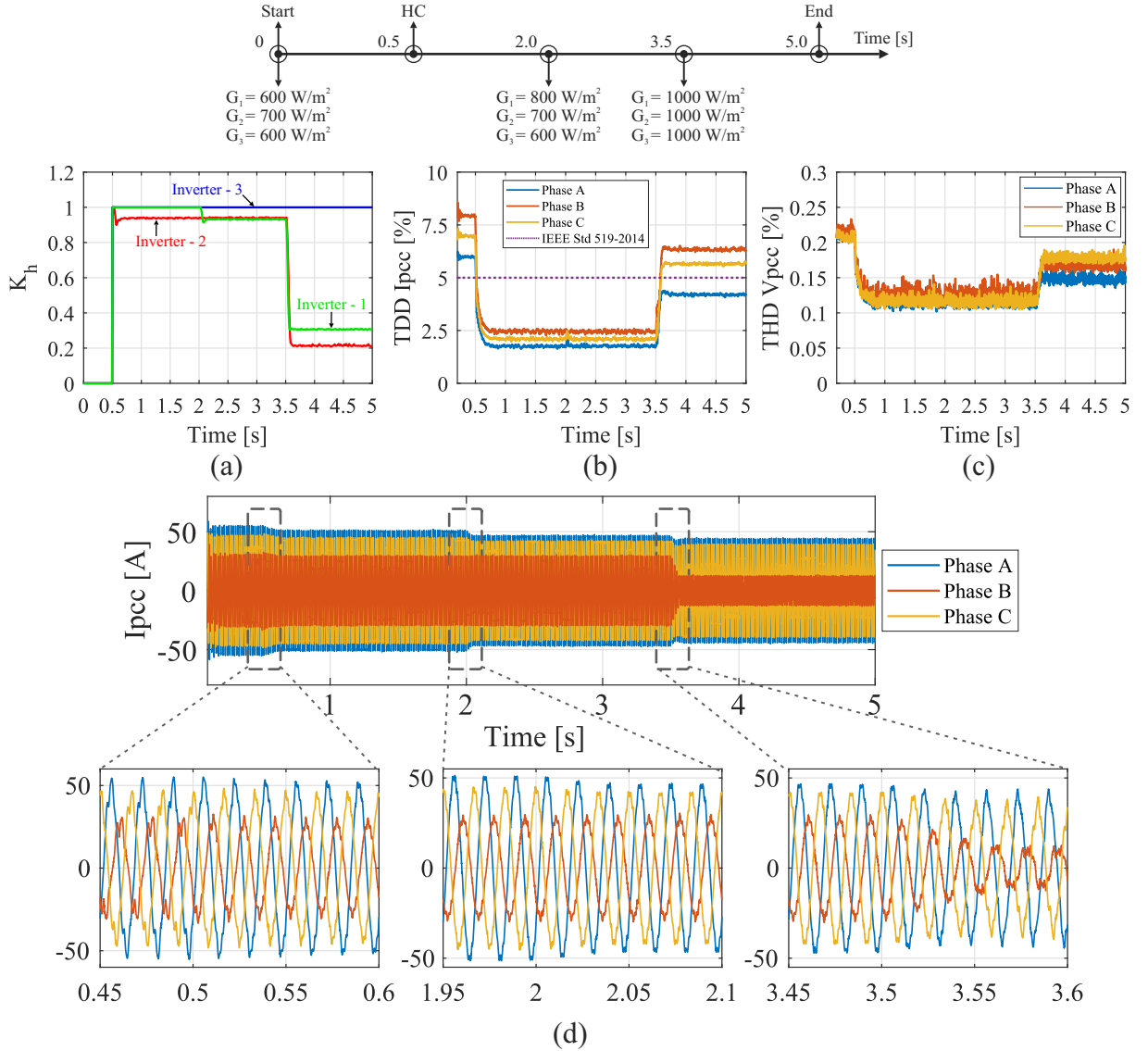


Figure 18 – Local current-based HC strategy evaluation: (a) Compensation factor K_h . (b) TDD of the PCC current i_{pcc} . (c) THD of the PCC voltage v_{pcc} . (d) PCC current dynamic.

$K_{h,1} = 0.30$ and $K_{h,2} = 0.21$, respectively. However, the oversized PV inverter 3 still have current margin for full harmonic compensation. The effects of this variation is an increase on the PCC current TDD and PCC voltages THD. Only the phase A remains the TDD value below the recommended 5%. It is observed a more distorted behaviour from the i_{pcc} waveforms, since the fundamental current supply reduces and the harmonic current supply increases.

The PV inverters output current ($i_{s,1}$, $i_{s,2}$ and $i_{s,3}$) dynamic are shown in Fig. 19. As highlighted in the figure, the inverters current peak does not exceed their limit values, except during some fundamental cycles in transient events of solar irradiance change. The current limits for the inverters 1, 2 and 3 ($I_{m,1}$, $I_{m,2}$ and $I_{m,3}$) are represented by the dashed lines in the graphics. Besides, the PV inverters output current TDD values at

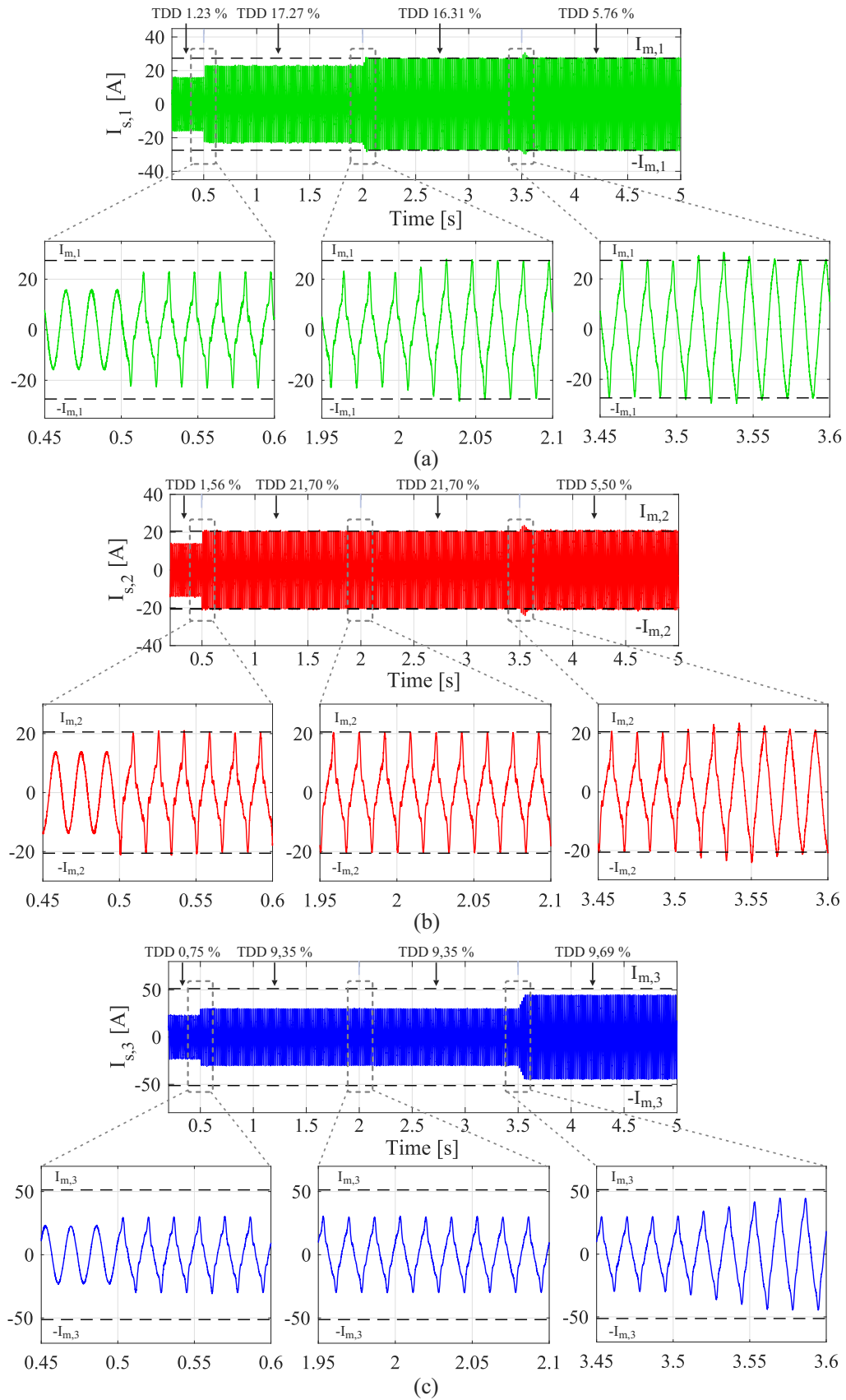


Figure 19 – Local current-based HC strategy evaluation: (a) Inverter-1 current dynamic. (b) Inverter-2 current dynamic. (c) Inverter-3 current dynamic.

each time interval are indicated in the graphics. As expected, when the HC capability is performed the harmonic distortion on the PV inverter increases. For instance, the TDD of the output currents of PV systems 1, 2 and 3 increased from 1.23% to 17.27%, 1.56% to 21.70% and 0.75% to 9.35%, respectively. In fact, this current distortions have effects on the PV inverter lifetime. However, these discussions will be left to future works.

4.2.2 Local Voltage-based HC Strategy Evaluation

Similar to the previous analysis, Fig. 20 shows the results for the local voltage-based HC strategy in terms of the PCC variables. When the HC is enabled in 0.5 s, the inverters 1 and 3 have current margin for full harmonic compensation and the their compensation factor, $K_{h,1}$ and $K_{h,3}$, rapidly reaches unitary alue. On the other hand, the compensation factor for the inverter 2, $K_{h,2}$, has a slower response until stabilize around 0.92. Note that for the local voltage-based HC scheme, the harmonic current reference is produced by measuring the PoC voltage. Thus, the interaction between the harmonic current compensated by PV inverter and the effects on the PoC voltages may lead to slower time responses when compared to measure the harmonic current directly. Moreover, a fast transient peak is observed on the PCC currents and voltages at this moment, and further the TDD for i_{pcc} reduces to values below 5%.

In 2 s, when the solar irradiance on the PV system 1 changes to 800 W/m², inverter 1 reduces its harmonic compensation to a factor $K_{h,1}$ around 0.82. Compared to the previous analyzed HC strategy, the dynamic response at this moment is slower and the compensation factor is smaller. As the harmonic current reference generation procedure is different, the contribution in terms of current peak value between the voltage-based and current-based strategies may be different, which affects the K_h value. Thus, even for the same conditions, the compensation factor obtained for the two techniques may be different. Again, at this moment, the effects of this solar irradiance change is almost imperceptible in terms of the TDD and THD on the PCC, while the fundamental current supplied by the upstream grid reduces.

Furthermore, in 3.5 s, when the solar irradiance in all PV system reaches 1000 W/m², the HC is drastically reduced in the inverters 1 and 2 by setting the factor $K_{h,1}$ and $K_{h,2}$ to 0.054 and 0.035, respectively. Meanwhile, the inverter 3 still has current margin to maintain $K_{h,3}$ equals 1. As result, the PCC currents TDD increases from 1.23% to 4.02%, 1.70% to 6.04% and 1.45% to 6.16% for phases *A*, *B* and *C*, respectively. In the same phase sequence, PCC voltages THD increases from 0.087% to 0.131%, 0.106% to 0.156%, 0.089% to 0.180%. Especially for the phase *C*, the worsening in power quality is more evident since two PV systems responsible for HC in this phase are practically disabled.

Finally, Fig. 21 shows the PV inverters output current dynamic highlighting the inverters current limit and the output current TDD at each time interval. Its noteworthy

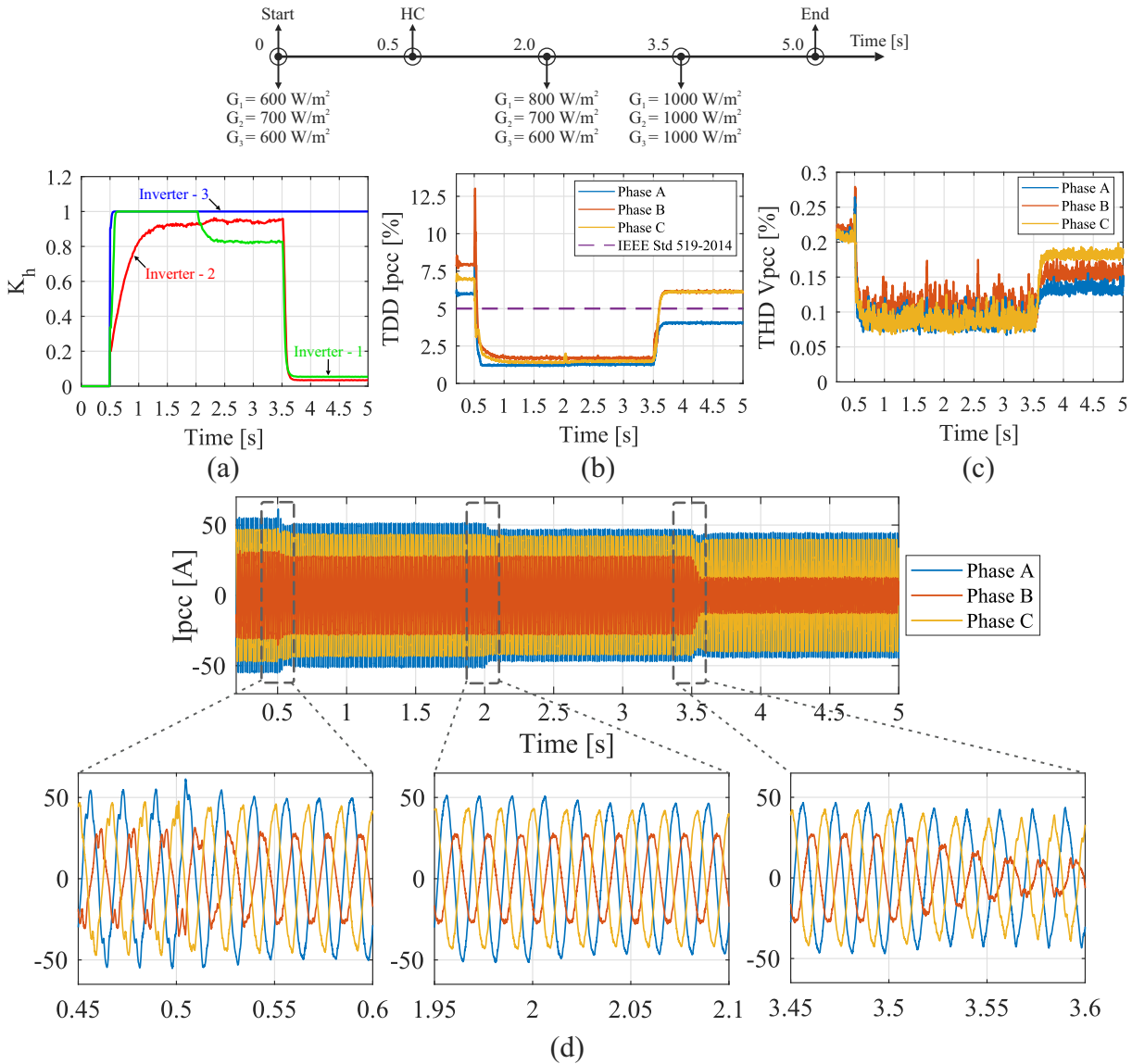


Figure 20 – Local voltage-based HC strategy evaluation: (a) Compensation factor K_h . (b) TDD of the PCC current i_{pcc} . (c) THD of the PCC voltage v_{pcc} . (d) PCC current dynamic.

that, when the HC is enabled in 0.5 s, a current peak is observed in $i_{s,1}$, $i_{s,2}$ and $i_{s,3}$. The effects of this transient behaviour are felt in the voltage and current of the PCC. However, the DS algorithm is capable of maintain the PV inverter within their current limits, except during a few fundamental cycles when transient events occur.

4.3 Chapter Closure

In this chapter, the case study system was evaluated for the two analyzed harmonic compensation strategies in terms of power quality improvements and dynamic response. The main results are synthesized by the comparative Table 6. The symbols (++), (+) and (-) are used to compare the figures of merit from the best to the worst performance, while

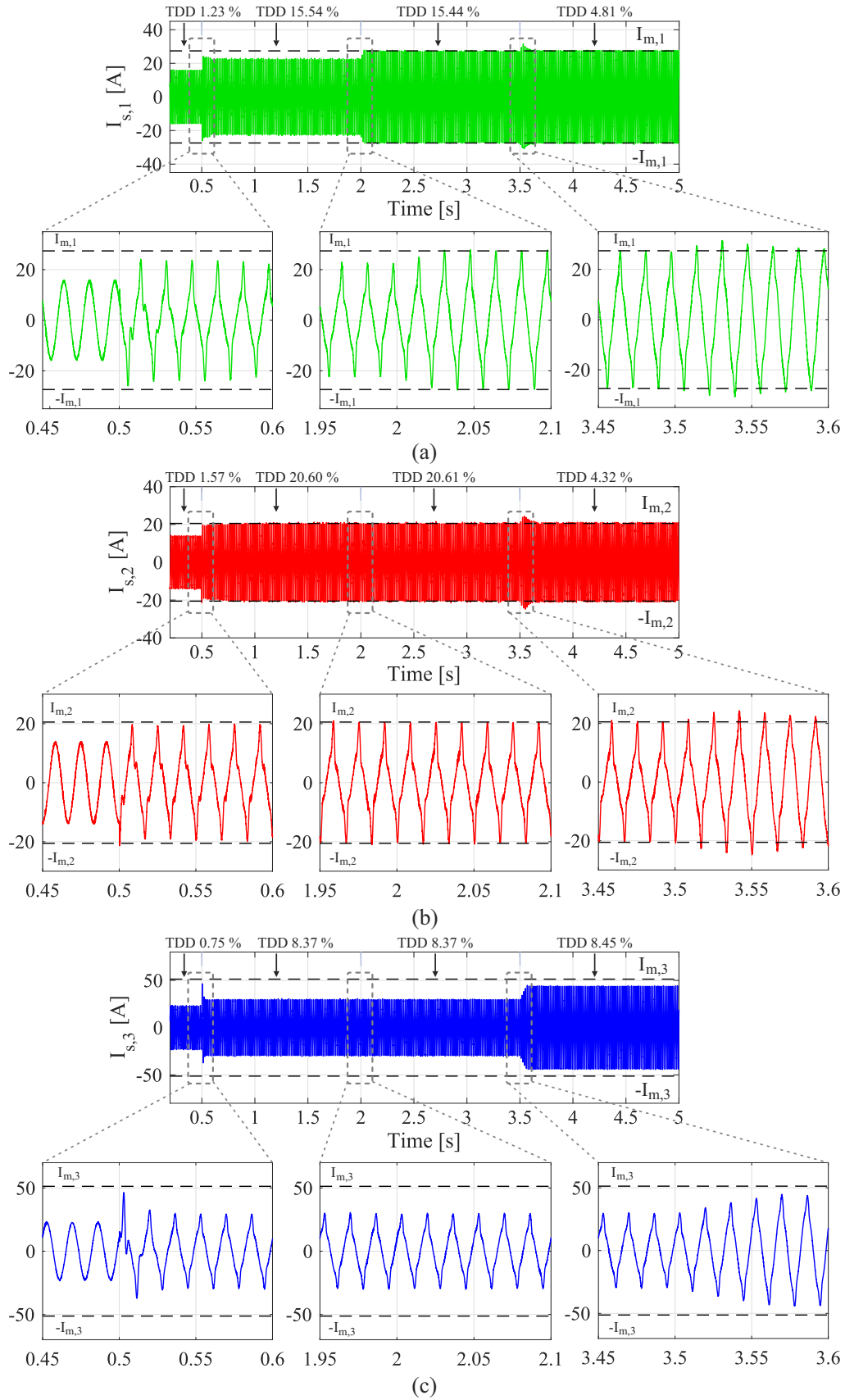


Figure 21 – Local voltage-based HC strategy evaluation: (a) Inverter-1 current dynamic. (b) Inverter-2 current dynamic. (c) Inverter-3 current dynamic.

the symbol (\approx) means equal performance. For stiff grids conditions, the local current-based HC scheme achieved better compensation result in terms of the currents TDD and voltages THD on the PCC, while for weak grids conditions the local voltage-based HC scheme stood out. It is noteworthy that the voltage-based HC strategy sees the distortions on the voltage of the inverter PoC. Any uncompensated harmonic current within the distribution grid may affect the voltage seen by the inverter, since the voltage is a global quantity at the transformer secondary side. On the other hand, the current-based HC strategy is only capable of compensate the harmonic currents at the specific PoC of each inverter. Therefore, in weak grid conditions, where the distortions on the voltage are higher, the voltage-based strategy may lead to better harmonic compensation performance.

The dynamic response evaluation refers to the response time and transient behaviour. In this context, the local voltage-based HC strategy presented poorer results with peak currents when the technique is enabled and slower time response. The computational burden evaluated in terms of harmonic detector requirements, number of controllers and dynamic saturation algorithm requirements is basically the same for both techniques. Moreover, as aforementioned, the local voltage-based HC scheme is susceptible to instability in view of the gain K_v value. At last, the local current-based HC scheme requires hardware changes for measuring the local nonlinear load current.

Table 6 – Comparison between the HC techniques.

Requirements	Local current-based HC scheme	Local voltage-based HC scheme
HC capacity into stiff grids conditions	++	+
HC capacity into weak grids conditions	+	++
Dynamic response	+	-
Computational burden	\approx	\approx
Susceptible to instability	+	-
Hardware changes	Yes	No

5 Conclusions

Previous chapters compared different harmonic compensation techniques applied to single-phase PV inverters in a case study system. This chapter summarizes the main contributions of this undergraduate thesis and possible future developments.

In this research project, the main focus is on evaluate the effects of two harmonic compensation strategies for single-phase grid-connected PV inverters in a low-voltage three phase radial distribution line. The main subjects of this work can be divided into three categories: (a) Benchmarking of the local current-based and local voltage-based HC strategies applied to PV systems in terms of control, covered in Chapter 2. (b) Case study aspects and configuration, addressed in Chapter 3. (c) Comparative evaluation of the HC strategies into the case study system, approached in Chapter 4.

The main contributions of this research project were presented in Chapter 1. The conclusions regarding them can be summarized as follows:

Implementation and study of the partial harmonic compensation applied to multiple PV systems using a dynamic saturation algorithm

The partial harmonic compensation for two strategies with a dynamic saturation algorithm for three single-phase PV systems was presented for a low-voltage three-phase radial distribution line with local nonlinear loads. Since each PV system was connected in two different phases of the line, the results on the point of common coupling power quality depends on the PV systems idle current margin.

Methodology to adjust the compensation gain for a voltage-based harmonic compensation strategy

The methodology for adjust the compensation gain K_v for local voltage-based harmonic compensation was based on the grid impedance stability analysis with the objective to ensure a stable operation. For the case study system, the K_v value chosen was 2.6 in order to ensure a stable operation in grid inductance range from 0.1 mH to 10 mH. The results showed that the for the analyzed grid impedances the technique stability was ensured. It is important to note that the analyzed grid impedance range is typical of distribution systems. For different grid impedance range and X/R ratio, new analyses should be developed.

Comparison between a current-based and a voltage-based harmonic compensation strategy applied to PV inverters in a case study system

In this work, the comparison between the current-based and the voltage-based harmonic compensation strategies applied to PV inverters were performed in terms of the

case study radial line. The simulation results shows that the power quality improvements depends on the grid impedance condition. In a weak grid condition, the local current-based HC reduces the TDD of the per-phase PCC currents in approximately 65% and the voltage current-based HC reduces this TDD in approximately 85%. In a stronger grid condition, the local current-based HC reduces the TDD of the per-phase PCC currents in approximately 75% and the voltage current-based HC reduces this TDD in approximately 64%. The dynamic responses for the voltage-based strategy were worse than for the current-based strategy in the analyzed condition. The computational burden defined in terms of harmonic detection requirements, number of current controllers and dynamic saturation algorithm requirements was essentially the same for both harmonic compensation strategies. Since, the local voltage-based harmonic compensation strategy depends on the compensation gain adjustment, it is more susceptible to instability if the correct methodology is not followed. Finally, the current-based strategy requires hardware changes that may limit its application.

5.1 Research Perspectives

Despite many aspects were documented in this undergraduate thesis, improvements and new studies can be performed. From the author point of view, the following studies can be approached in future investigations:

1. Validation of the comparison between harmonic compensation strategies in a experimental setup with a two-stage single-phase inverter;
2. Evaluation of the reduction on distribution lines losses/distortion power circulating into the line;
3. Evaluation and comparison on the additional thermal stress suffer by the converters when the harmonic compensation service is performed using the two discussed harmonic compensation strategies;
4. Evaluation of the system when reactive compensation service is performed together with the two discussed harmonic compensation strategies.

The possibilities for further research derived from this thesis are many. The author expects that this research project does not stop in this document.

References

- Abu-Rub, H.; Malinowski, M.; Al-Haddad, K. Photovoltaic energy conversion systems. In: _____. *Power Electronics for Renewable Energy Systems, Transportation and Industrial Applications*. [S.l.: s.n.], 2014. p. 160–198. [28](#), [29](#)
- Acuña, P. et al. Improved active power filter performance for renewable power generation systems. *IEEE Transactions on Power Electronics*, v. 29, n. 2, p. 687–694, 2014. [29](#)
- Akagi, H. Control strategy and site selection of a shunt active filter for damping of harmonic propagation in power distribution systems. *IEEE Transactions on Power Delivery*, v. 12, n. 1, p. 354–363, 1997. [32](#), [45](#)
- Akagi, H.; Fujita, H.; Wada, K. A shunt active filter based on voltage detection for harmonic termination of a radial power distribution line. *IEEE Transactions on Industry Applications*, v. 35, n. 3, p. 638–645, 1999. [32](#), [45](#)
- Akagi, H.; Kanazawa, Y.; Nabae, A. Instantaneous reactive power compensators comprising switching devices without energy storage components. *IEEE Transactions on Industry Applications*, IA-20, n. 3, p. 625–630, 1984. [32](#)
- Amorim, W. C. S. et al. Comparison of current grid controllers in a dg inverter with grid harmonic distortion. In: *2018 13th IEEE International Conference on Industry Applications (INDUSCON)*. [S.l.: s.n.], 2018. p. 194–201. [39](#)
- Asiminoaei, L. et al. A digital controlled pv-inverter with grid impedance estimation for ens detection. *IEEE Transactions on Power Electronics*, v. 20, n. 6, p. 1480–1490, 2005. [57](#)
- Asiminoael, L.; Blaabjerg, F.; Hansen, S. Detection is key - harmonic detection methods for active power filter applications. *IEEE Industry Applications Magazine*, v. 13, n. 4, p. 22–33, 2007. [32](#)
- Bialasiewicz, J. T. Renewable energy systems with photovoltaic power generators: Operation and modeling. *IEEE Transactions on Industrial Electronics*, v. 55, n. 7, p. 2752–2758, 2008. [29](#)
- Blaabjerg, F. et al. Overview of control and grid synchronization for distributed power generation systems. *IEEE Transactions on Industrial Electronics*, v. 53, n. 5, p. 1398–1409, 2006. [28](#)
- Blaabjerg, F. et al. Overview of control and grid synchronization for distributed power generation systems. *Industrial Electronics, IEEE Transactions on*, v. 53, p. 1398 – 1409, 11 2006. [38](#)
- Blaabjerg, F. et al. Distributed power-generation systems and protection. *Proceedings of the IEEE*, v. 105, n. 7, p. 1311–1331, 2017. [28](#)
- Bojoi, R. I. et al. Enhanced power quality control strategy for single-phase inverters in distributed generation systems. *IEEE Transactions on Power Electronics*, v. 26, n. 3, p. 798–806, 2011. [31](#)

- Bonaldo, J. P.; Morales Paredes, H. K.; Pomilio, J. A. Control of single-phase power converters connected to low-voltage distorted power systems with variable compensation objectives. *IEEE Transactions on Power Electronics*, v. 31, n. 3, p. 2039–2052, 2016. 30, 31
- Buso, S.; Mattavelli, P. *Digital Control in Power Electronics*. 2nd. ed. [S.l.]: Morgan and Claypool Publishers, 2015. ISBN 1627057536. 40
- Canadian Solar. *Canadian solar website*. 2021. Disponível em: <<https://www.canadiansolar.com/>>. 28
- Carrasco, J. M. et al. Power-electronic systems for the grid integration of renewable energy sources: A survey. *IEEE Transactions on Industrial Electronics*, v. 53, n. 4, p. 1002–1016, 2006. 28
- Chen, H. et al. Analysis and design of enhanced dft-based controller for selective harmonic compensation in active power filters. In: *2018 IEEE Applied Power Electronics Conference and Exposition (APEC)*. [S.l.: s.n.], 2018. p. 1305–1309. 32
- Ciobotaru, M.; Teodorescu, R.; Blaabjerg, F. A new single-phase pll structure based on second order generalized integrator. In: *2006 37th IEEE Power Electronics Specialists Conference*. [S.l.: s.n.], 2006. p. 1–6. ISSN 2377-6617. 39
- Ciobotaru, M. et al. Online grid impedance estimation for single-phase grid-connected systems using pq variations. In: *2007 IEEE Power Electronics Specialists Conference*. [S.l.: s.n.], 2007. p. 2306–2312. 57
- Corradini, L. et al. The digital control loop. In: _____. *Digital Control of High-Frequency Switched-Mode Power Converters*. [S.l.: s.n.], 2015. p. 51–78. 43
- Das, J. C. Passive filters - potentialities and limitations. *IEEE Transactions on Industry Applications*, v. 40, n. 1, p. 232–241, 2004. 30
- De la Rosa, F. C. *Harmonics and Power Systems*. Boca Raton: CRC Press, 2006. 208 p. 29, 30
- Esrám, T.; Chapman, P. L. Comparison of photovoltaic array maximum power point tracking techniques. *IEEE Transactions on Energy Conversion*, v. 22, n. 2, p. 439–449, 2007. 38
- Gajanayake, C. J. et al. Z-source-inverter-based flexible distributed generation system solution for grid power quality improvement. *IEEE Transactions on Energy Conversion*, v. 24, n. 3, p. 695–704, 2009. 34
- Gomes, C. C.; Cupertino, A. F.; Pereira, H. A. Damping techniques for grid-connected voltage source converters based on lcl filter: An overview. *Renewable and Sustainable Energy Reviews*, v. 81, p. 116 – 135, 2018. ISSN 1364-0321. 39
- He, J. et al. Active harmonic filtering using current-controlled, grid-connected dg units with closed-loop power control. *IEEE Transactions on Power Electronics*, v. 29, n. 2, p. 642–653, 2014. 32, 33

- He, J.; Li, Y. W.; Munir, M. S. A flexible harmonic control approach through voltage-controlled dg-grid interfacing converters. *IEEE Transactions on Industrial Electronics*, v. 59, n. 1, p. 444–455, 2012. 31, 46
- Hoffmann, N. et al. Digital current control in a rotating reference frame - part i: System modeling and the discrete time-domain current controller with improved decoupling capabilities. *IEEE Transactions on Power Electronics*, v. 31, n. 7, p. 5290–5305, 2016. 43
- Holmes, D. G.; Lipo, T. A. Modulation of singlephase voltage source inverters. In: _____. *Pulse Width Modulation for Power Converters: Principles and Practice*. [S.l.: s.n.], 2003. p. 155–213. 39
- IEC. *IEC 61727: Photovoltaic (PV) Systems - Characteristics of the Utility Interface*. 2004. 39
- IEEE Recommended Practice and Requirements for Harmonic Control in Electric Power Systems. *IEEE Std 519-2014 (Revision of IEEE Std 519-1992)*, p. 1–29, 2014. 30, 58
- IEEE Standard for Interconnection and Interoperability of Distributed Energy Resources with Associated Electric Power Systems Interfaces. *IEEE Std 1547-2018 (Revision of IEEE Std 1547-2003)*, p. 1–138, 2018. 46
- IRENA. *Renewable capacity highlights*. 2020. Disponível em: <https://irena.org/-/media/Files/IRENA/Agency/Publication/2020/Mar/IRENA_RE_Capacity_Highlights_2020.pdf?la=en&hash=B6BDF8C3306D271327729B9F9C9AF5F1274FE30B>. 13, 27, 28
- Jintakosonwit, P. et al. Implementation and performance of automatic gain adjustment in a shunt-active filter for harmonic damping throughout a power distribution system. *IEEE Transactions on Power Electronics*, v. 17, n. 3, p. 438–447, 2002. 32, 45
- Kouro, S. et al. Grid-connected photovoltaic systems: An overview of recent research and emerging pv converter technology. *IEEE Industrial Electronics Magazine*, v. 9, n. 1, p. 47–61, 2015. 27, 28
- Lee, T.; Cheng, P. Design of a new cooperative harmonic filtering strategy for distributed generation interface converters in an islanding network. *IEEE Transactions on Power Electronics*, v. 22, n. 5, p. 1919–1927, 2007. 31
- Lee, T.-L.; Li, J.-C.; Cheng, P.-T. Discrete frequency tuning active filter for power system harmonics. *IEEE Transactions on Power Electronics*, v. 24, n. 5, p. 1209–1217, 2009. 46
- Li, Y. W.; He, J. Distribution system harmonic compensation methods: An overview of dg-interfacing inverters. *IEEE Industrial Electronics Magazine*, v. 8, n. 4, p. 18–31, 2014. 32, 42, 46
- Liserre, M.; Teodorescu, R.; Blaabjerg, F. Stability of photovoltaic and wind turbine grid-connected inverters for a large set of grid impedance values. *IEEE Transactions on Power Electronics*, v. 21, n. 1, p. 263–272, 2006. 49
- Marafao, F. et al. Multi-task control strategy for grid-tied inverters based on conservative power theory. *IET Renewable Power Generation*, v. 9, p. 154–165, 03 2015. 30, 32

- Mastromauro, R. A. et al. A single-phase voltage-controlled grid-connected photovoltaic system with power quality conditioner functionality. *IEEE Transactions on Industrial Electronics*, v. 56, n. 11, p. 4436–4444, 2009. 29, 33
- Mousavi, S. Y. M. et al. Flexible compensation of voltage and current unbalance and harmonics in microgrids. *Energies*, v. 10, n. 10, 2017. ISSN 1996-1073. 31
- Munir, S.; Li, Y. W. Residential distribution system harmonic compensation using pv interfacing inverter. *IEEE Transactions on Smart Grid*, v. 4, n. 2, p. 816–827, 2013. 30
- Nie, C. et al. An enhanced control strategy for multiparalleled grid-connected single-phase converters with load harmonic current compensation capability. *IEEE Transactions on Industrial Electronics*, v. 65, n. 7, p. 5623–5633, 2018. 32
- Petrone, G. et al. Reliability issues in photovoltaic power processing systems. *IEEE Transactions on Industrial Electronics*, v. 55, n. 7, p. 2569–2580, 2008. 29
- PHB Solar. *PHB solar website*. 2021. Disponível em: <<https://www.energiasolarphb.com.br/>>. 28
- Pogaku, N.; Green, T. Harmonic mitigation throughout a distribution system: A distributed-generator-based solution. *Generation, Transmission and Distribution, IEE Proceedings-*, v. 153, p. 350 – 358, 06 2006. 32, 34
- Rauschenbach, H. S. *Solar Cell Array Design Handbook: The Principles and Technology of Photovoltaic Energy Conversion*. New York: Van Nostrand Reinhold, 1980. 549 p. 37
- REN 21. *Renewables 2020: Global Status Report*. 2020. Disponível em: <https://www.ren21.net/wp-content/uploads/2019/05/gsr_2020_full_report_en.pdf>. 13, 27
- Robert, A. et al. Guide for assessing the network harmonic impedance. In: *14th International Conference and Exhibition on Electricity Distribution. Part 1. Contributions (IEE Conf. Publ. No. 438)*. [S.l.: s.n.], 1997. v. 2, p. 3/1–310 vol.2. 57
- Rodríguez, P. et al. Multiresonant frequency-locked loop for grid synchronization of power converters under distorted grid conditions. *IEEE Transactions on Industrial Electronics*, v. 58, n. 1, p. 127–138, 2011. 32
- Savaghebi, M. et al. Secondary control for voltage quality enhancement in microgrids. *IEEE Transactions on Smart Grid*, v. 3, n. 4, p. 1893–1902, 2012. 42
- Savaghebi, M. et al. Adaptive virtual impedance scheme for selective compensation of voltage unbalance and harmonics in microgrids. In: *2015 IEEE Power Energy Society General Meeting*. [S.l.: s.n.], 2015. p. 1–5. 31
- Shynk, J. Adaptive iir filtering. *IEEE ASSP Magazine*, v. 6, n. 2, p. 4–21, 1989. 42
- Singh, B.; Al-Haddad, K.; Chandra, A. A review of active filters for power quality improvement. *IEEE Transactions on Industrial Electronics*, v. 46, n. 5, p. 960–971, 1999. 30
- SMA Solar Technology. *SMA Solar Technology website*. 2021. Disponível em: <<https://www.sma-south-america.com/pt.html>>. 28

- Tang, K. et al. Genetic algorithms and their applications. *IEEE Signal Processing Magazine*, v. 13, n. 6, p. 22–37, 1996. [42](#)
- Tang, Y. et al. Generalized design of high performance shunt active power filter with output lcl filter. *IEEE Transactions on Industrial Electronics*, v. 59, n. 3, p. 1443–1452, 2012. [31](#)
- Teodorescu, R.; Liserre, M.; Rodriguez, P. Photovoltaic inverter structures. In: _____. *Grid Converters for Photovoltaic and Wind Power Systems*. [S.l.: s.n.], 2007. p. 5–29. [28](#), [29](#), [31](#)
- Teodorescu, R.; Liserre, M.; Rodriguez, P. Photovoltaic inverter structures. In: _____. *Grid Converters for Photovoltaic and Wind Power Systems*. [S.l.: s.n.], 2007. p. 5–29. [39](#)
- Timbus, A. et al. Online grid impedance measurement suitable for multiple pv inverters running in parallel. In: *Twenty-First Annual IEEE Applied Power Electronics Conference and Exposition, 2006. APEC '06*. [S.l.: s.n.], 2006. p. 5 pp.–. [57](#)
- Timbus, A. V.; Teodorescu, R.; Rodriguez, P. Grid impedance identification based on active power variations and grid voltage control. In: *2007 IEEE Industry Applications Annual Meeting*. [S.l.: s.n.], 2007. p. 949–954. [57](#)
- Ting Qian et al. Adaptive saturation scheme to limit the capacity of a shunt active power filter. In: *Proceedings of 2005 IEEE Conference on Control Applications, 2005. CCA 2005*. [S.l.: s.n.], 2005. p. 1674–1679. [34](#)
- Torquato, R. et al. A comprehensive assessment of pv hosting capacity on low-voltage distribution systems. *IEEE Transactions on Power Delivery*, v. 33, n. 2, p. 1002–1012, 2018. [29](#)
- Villalva, M.; Gazoli, J.; Filho, E. Modeling and circuit-based simulation of photovoltaic arrays. In: *IEEE Transactions on Power Electronics*. [S.l.: s.n.], 2009. v. 14, p. 1244 – 1254. [37](#)
- Wada, K.; Fujita, H.; Akagi, H. Considerations of a shunt active filter based on voltage detection for installation on a long distribution feeder. *IEEE Transactions on Industry Applications*, v. 38, n. 4, p. 1123–1130, 2002. [32](#), [45](#)
- Wang, F. et al. Modeling and analysis of grid harmonic distortion impact of aggregated dg inverters. *IEEE Transactions on Power Electronics*, v. 26, n. 3, p. 786–797, 2011. [28](#)
- Wang, X. et al. Secondary voltage control for harmonics suppression in islanded microgrids. In: *2011 IEEE Power and Energy Society General Meeting*. [S.l.: s.n.], 2011. p. 1–8. [31](#)
- Wang, Y. F.; Li, Y. W. Three-phase cascaded delayed signal cancellation pll for fast selective harmonic detection. *IEEE Transactions on Industrial Electronics*, v. 60, n. 4, p. 1452–1463, 2013. [32](#)
- Williams, A. B.; Taylor, F. J. *Electronic Filter Design Handbook*. 4th. ed. [S.l.]: McGRAW-HILL, 1995. 766 p. ISBN 1627057536. [42](#)
- Wu, X. H.; Panda, S. K.; Xu, J. X. Design of a plug-in repetitive control scheme for eliminating supply-side current harmonics of three-phase pwm boost rectifiers under generalized supply voltage conditions. *IEEE Transactions on Power Electronics*, v. 25, n. 7, p. 1800–1810, 2010. [33](#)

Xavier, L.; Cupertino, A.; Pereira, H. Ancillary services provided by photovoltaic inverters: Single and three phase control strategies. *Computers & Electrical Engineering*, v. 70, 03 2018. 29, 31, 33

Xavier, L. S. *Harmonic Current Compensation Applied in Single-Phase Photovoltaic Systems*. Dissertação (Mestrado) — Federal University of Minas Gerais - UFMG, 2018. 38, 57

Xavier, L. S. et al. Partial harmonic current compensation for multifunctional photovoltaic inverters. *IEEE Transactions on Power Electronics*, v. 34, n. 12, p. 11868–11879, 2019. 34, 50

Xing, H.; Ploeg, J.; Nijmeijer, H. Padé approximation of delays in cooperative acc based on string stability requirements. *IEEE Transactions on Intelligent Vehicles*, v. 1, n. 3, p. 277–286, 2016. 43

Yang, Y. *Advanced Control Strategies to Enable a More Wide-Scale Adoption of Single-Phase Photovoltaic Systems*. Tese (Doutorado), aug 2014. 38, 40

Yang, Y. et al. Power control flexibilities for grid-connected multi-functional photovoltaic inverters. *IET Renewable Power Generation*, PP, p. 1–10, 04 2016. 29

Yang, Y.; Wang, H.; Blaabjerg, F. Reactive power injection strategies for single-phase photovoltaic systems considering grid requirements. In: *2014 IEEE Applied Power Electronics Conference and Exposition - APEC 2014*. [S.l.: s.n.], 2014. p. 371–378. 33

Yang, Y.; Zhou, K.; Blaabjerg, F. Frequency adaptability of harmonics controllers for grid-interfaced converters. *International Journal of Control*, Taylor and Francis, v. 90, n. 1, p. 3–14, 2017. 38

YAZDANI, A.; IRAVANI, R. Grid-imposed frequency vsc system: Control in -frame. In: _____. *Voltage-Sourced Converters in Power Systems: Modeling, Control, and Applications*. [S.l.: s.n.], 2010. p. 160–203. 40

Yepes, A. G. *Digital Resonant Current Controllers for Voltage Source Converters*. Tese (Doutorado), dec 2011. 40, 41, 55

Yepes, A. G. et al. Analysis and design of resonant current controllers for voltage-source converters by means of nyquist diagrams and sensitivity function. *IEEE Transactions on Industrial Electronics*, v. 58, n. 11, p. 5231–5250, 2011. 33

Yunwei Li; Vilathgamuwa, D. M.; Poh Chiang Loh. Design, analysis, and real-time testing of a controller for multibus microgrid system. *IEEE Transactions on Power Electronics*, v. 19, n. 5, p. 1195–1204, 2004. 31

Zangeneh Bighash, E. et al. Adaptive-harmonic compensation in residential distribution grid by roof-top pv systems. *IEEE Journal of Emerging and Selected Topics in Power Electronics*, v. 6, n. 4, p. 2098–2108, 2018. 30

Zhang, Y. *Voltage support in weak grids: local control of grid-connected power electronic converters*. Tese (Doutorado) — Electrical Engineering, nov. 2019. Proefschrift. 42, 47, 48

- Zhang, Y. et al. Integrated local control of active power and voltage support for three-phase three-wire converters. In: *2019 IEEE 15th Brazilian Power Electronics Conference and 5th IEEE Southern Power Electronics Conference (COBEP/SPEC)*. [S.l.: s.n.], 2019. p. 1–6. [32](#), [33](#)
- Zhao, X. et al. A unified voltage harmonic control strategy for coordinated compensation with vcm and ccm converters. *IEEE Transactions on Power Electronics*, v. 33, n. 8, p. 7132–7147, 2018. [31](#)
- Zhao, X. et al. A voltage feedback based harmonic compensation strategy for current-controlled converters. *IEEE Transactions on Industry Applications*, v. 54, n. 3, p. 2616–2627, 2018. [32](#)
- Zobaa, A. F.; Abdel Aleem, S. H. E. A new approach for harmonic distortion minimization in power systems supplying nonlinear loads. *IEEE Transactions on Industrial Informatics*, v. 10, n. 2, p. 1401–1412, 2014. [30](#)
- Zou, Z.; Wang, Z.; Cheng, M. Modeling, analysis, and design of multifunction grid-interfaced inverters with output lcl filter. *IEEE Transactions on Power Electronics*, v. 29, n. 7, p. 3830–3839, 2014. [31](#)